

5-2017

Towards Computer Aided Management of Kidney Disease

Vipul Pai Raikar

Clemson University, vpai@g.clemson.edu

Follow this and additional works at: https://tigerprints.clemson.edu/all_dissertations

Recommended Citation

Pai Raikar, Vipul, "Towards Computer Aided Management of Kidney Disease" (2017). *All Dissertations*. 1929.
https://tigerprints.clemson.edu/all_dissertations/1929

This Dissertation is brought to you for free and open access by the Dissertations at TigerPrints. It has been accepted for inclusion in All Dissertations by an authorized administrator of TigerPrints. For more information, please contact kokeefe@clemson.edu.

TOWARDS COMPUTER AIDED MANAGEMENT OF KIDNEY DISEASE

A Dissertation
Presented to
the Graduate School of
Clemson University

In Partial Fulfillment
of the Requirements for the Degree
Doctor of Philosophy
Bioengineering

by
Vipul Pai Raikar
May 2017

Accepted by:
Dr. David Kwartowitz, Committee Chair
Dr. Delphine Dean
Dr. Donald House
Dr. Bruce Gao

Abstract

Autosomal dominant polycystic kidney disease (ADPKD) is the fourth most common cause of kidney transplant worldwide accounting for 7-10% of all cases. Although ADPKD usually progresses over many decades, accurate risk prediction is an important task. Identifying patients with progressive disease is vital to providing new treatments being developed and enable them to enter clinical trials for new therapy. Among other factors, total kidney volume (TKV) is a major biomarker predicting the progression of ADPKD. Consortium for Radiologic Imaging Studies in Polycystic Kidney Disease (CRISP) have shown that TKV is an early, and accurate measure of cystic burden and likely growth rate. It is strongly associated with loss of renal function. While ultrasound (US) has proven as an excellent tool for diagnosing the disease; monitoring short-term changes using ultrasound has been shown to not be accurate. This is attributed to high operator variability and reproducibility as compared to tomographic modalities such as CT and MR (Gold standard). Ultrasound has emerged as one of the standout modalities for intra-procedural imaging and with methods for spatial localization has afforded us the ability to track 2D ultrasound in the physical space in which it is being used. In addition to this, the vast amount of recorded tomographic data can be used to generate statistical shape models that allow us to extract clinical value from archived image sets.

Renal volumetry is of great interest in the management of chronic kidney dis-

eases (CKD). In this work, we have implemented a tracked ultrasound system and developed a statistical shape model of the kidney. We utilize the tracked ultrasound to acquire a stack of slices that are able to capture the region of interest, in our case kidney phantoms, and reconstruct 3D volume from spatially localized 2D slices. Approximate shape data is then extracted from this 3D volume using manual segmentation of the organ and a shape model is fit to this data. This generates an instance from the shape model that best represents the scanned phantom and volume calculation is done on this instance. We observe that we can calculate the volume to within 10% error in estimation when compared to the gold standard volume of the phantom.

Dedication

I dedicate this work to my family. My grandmother, Sulochana for always teaching me the importance of learning. To my late grandfather Venkatesh, who taught me to have a vivid imagination. To my parents, Madhura and Shrihari, who always put their children before everything else. Words can not express the gratitude I feel towards you. And to my brother Piyush for being my partner in crime and for his unconditional love and loyalty. Thank you!

Acknowledgments

Firstly, I would like to extend my utmost gratitude to my advisor Dr. David Kwartowitz for his guidance and encouragement during my PhD. I will cherish our conversations on a myriad of topics ranging from music to technology and everything in between. Thank you to my committee members, Dr. Donald House and Dr. Bruce Gao for your words of encouragement. I would like to especially thank Dr. Delphine Dean for not only being my committee member, but also for giving me the opportunity to serve as her teaching assistant. Your enthusiasm for teaching and positivity are infectious. Your words, “There is no need to panic!” will always stay with me. Go team!

I would like to extend my thanks to Dr. Martine LaBerge for her support and kind words of encouragement as well as members of the Bioengineering department. I would especially like to thank Ms. Maria Torres for always leaving her door open to any student that needed help. Her kindness and constant encouragement have had a huge influence on not only me, but every student that has been part of this department. I would like to thank Ms. Melissa McCullough and my fellow TA's Tyler, Hetal and Lucas for their friendship and making teaching so much enjoyable.

Two families deserve a special thanks. The Mefleh family, Jeanne, Nedal, Ahmed, Hashim, Fuad and Maliha. Their friendship, love and kindness will always stay with me where ever I go. Thank you for making me part of your brood. The

Hodarkar family. My aunt Bharati and uncle Sanjay, and cousins Rhea and Pooja. I can't begin to express how grateful I am to you for your unconditional love and letting me make New York my home away from home. Thank you Rhea and Pooj for my permanent spot on the basement couch and for making me fall in love with NYC. Our times of gallivanting around the city have been a prime highlight of my time in the states.

I would be remiss if I didn't mention the amazing people I have met here in Clemson and my friends back home. Krishna, Fadhira, Nikeetha, Romit, Namrata, Nick, Waqas, Tigran, Vratika, Ajit, Agraj, Rayesh, Vishi: Thank you for your affection, memories and friendships to last a life time. I would like to also mention three very special friends Hadi, Fuad and Maria: Thank you for believing in me and always encouraging me, for your loyalty and for the profound positive impact you guys have had on me.

I would finally like to thank my mom, dad and my brother: without you none of this would have been possible. Thank you!

Table of Contents

Title Page	i
Abstract	ii
Dedication	iv
Acknowledgments	v
List of Tables	viii
List of Figures	ix
1 Introduction	1
1.1 Autosomal Dominant Polycystic Kidney Disease (ADPKD): A Back-ground	1
1.2 Specific Aims	9
2 Development of a tracked freehand ultrasound system	11
2.1 Introduction	11
2.2 Methods	22
2.3 Summary	30
3 Development of statistical shape model of the human kidney . . .	32
3.1 Introduction	32
3.2 Methods	36
3.3 Results	44
3.4 Summary	50
4 Statistical shape modeling based renal volume measurement using tracked ultrasound	52
4.1 Introduction	52
4.2 Methods	54
4.3 Results	61
5 Conclusion and Future Work	67

Appendices	71
A Using curvelet transform for edge detection and segmentation of tissue	72
Bibliography	84

List of Tables

2.1	Summary of 3D scanning methods, acquisition modes and disadvantages.	17
2.2	Actual and measured dimensions of cuboid using tracked ultrasound .	30
2.3	Actual and measured dimensions of cylinder using tracked ultrasound	30
4.1	Volume calculated from segmentations done by subjects and the corresponding absolute percentage difference in volume from gold standard volume of 175 mL for Phantom 1	61
4.2	Volume calculated from segmentations done by subjects and the corresponding absolute percentage difference in volume from gold standard volume of 266 mL for Phantom 2	62
4.3	Volume calculated from segmentations done by subjects and the corresponding absolute percentage difference in volume from gold standard volume of 200 mL for Phantom 3	63

List of Figures

1.1	Illustration of the early stages of cyst formation and enlargement with fibrotic tissue deposition	2
1.2	Cyst formation at the level of the cell, nephron, and kidney. Defects in the genes encoding PKD1 or PKD2 lead to aberrant gene transcription, cell proliferation, and ion secretion, which in turn result in the formation of fluid-filled cysts. As cysts balloon out from individual nephrons, their collective effect leads to the displacement of the normal renal parenchyma and the formation of a cyst-filled kidney with reduced functional capacity. Cyst formation at the level of the cell, nephron, and kidney. Defects in the genes encoding PKD1 or PKD2 lead to aberrant gene transcription, cell proliferation, and ion secretion, which in turn result in the formation of fluid-filled cysts. As cysts balloon out from individual nephrons, their collective effect leads to the displacement of the normal renal parenchyma and the formation of a cyst-filled kidney with reduced functional capacity	3
1.3	Autosomal Dominant Polycystic Kidney (a) as compared to a healthy kidney, (b) imaged under ultrasound and (c) imaged under MRI . . .	9
2.1	Mechanical tracking system FARO arm (a), Electromagnetic tracking system NDI Aurora (b), Optical tracking system NDI Polaris and Vicra	13
2.2	Software components of PLUS toolkit	19
2.3	Sonosite M-Turbo with 6-15MHz linear array probe	22
2.4	Polaris active tool marker wiring matrix	23
2.5	Plot of temporal offset for calibration at imaging depth of 6 cms before and after applying offset. The moving signal represents tracker pose data and fixed signal represents imaging data	24
2.6	Illustration of coordinate system and transforms involved in a freehand ultrasound system	26
2.7	Illustration of Z-wire phantom used in freehand ultrasound calibration	27
3.1	Screen capture of the segmentation workflow in Mimics	36
3.2	Kidney datasets before and after rigid CPD alignment	39
3.3	Reference kidney shape generated iteratively	41

3.4	Samples from PCA shape model with samples from first three modes representing $\pm 3SD$	44
3.5	Metrics for assessment of the shape model	45
3.6	Metrics for assessment of the extended shape model	46
3.7	Comparison of compactness between PCA model and Extended model	47
3.8	Comparison of generalization between PCA model and Extended model	48
3.9	Comparison of specificity between PCA model and Extended model .	49
4.1	Kidney phantoms made from Smooth-on Ecoflex0030.	55
4.2	Kidney phantom under ultrasound showing partial surface	55
4.3	Kidney segmentation in 3D slicer. Bottom image shows manual segmentation masks	57
4.4	Segmentation mask and the deformed sphere fit to the mask to generate a closed mesh representation	58
4.5	Illustration of a unit tetrahedron used for calculating the volume of a triangular mesh	59
4.6	Workflow for volume calculation	60
4.7	Scatter plot showing the volumes obtained by segmenting the same phantom twice by subjects	65
1	Edge fragment is represented by multi-scale curvelets. Unaligned coefficients are tending towards zero	73
2	Algorithmic representation of ultrasound segmentation scheme	76
3	Directional fields along the feature. In top image the field exhibits a high degree of alignment along the edge as opposed to the curvelets away from the edge in the bottom image	78
4	Illustration of combined intensity-direction profile	79
5	Segmented edge overlaid on original image (top). Magnified view of the edge showing control points that can be used for various curve fitting methods (bottom)	80
6	The left column shows the set of input images (a), (c), (e), and (g) and the right column shows the segmented edge shapes over laid on the original images (b), (d), (f), and (h)	81

Chapter 1

Introduction

1.1 Autosomal Dominant Polycystic Kidney Disease (ADPKD): A Background

Autosomal dominant polycystic kidney disease (ADPKD) is the fourth leading cause of end-stage renal disease in adults. It accounts for 7-10 % of all patients for renal replacement therapy worldwide and is the most common inherited kidney disease. In the United States, ADPKD affects 300,000 to 600,000 individuals. One in every twenty cases of end-stage renal disease (ESRD) is caused due to ADPKD[50]. It is caused by the mutations in the PDK1 gene or the PKD2 gene located on chromosome 16 and 4 respectively. These genes are responsible for proteins polycystin-1 and polycystin-2. The mutation in PDK genes causes signal dysregulation and eventual cystogenesis due to higher levels of cyclic adenosine monophosphate (cAMP)[42, 24]. It is a progressive disorder that begins with a relatively small number of cystic renal tubules which expand over time. Cystogenesis is triggered with the levels of polycystin-1 and polycystin-2 fall below the threshold that is necessary to maintain

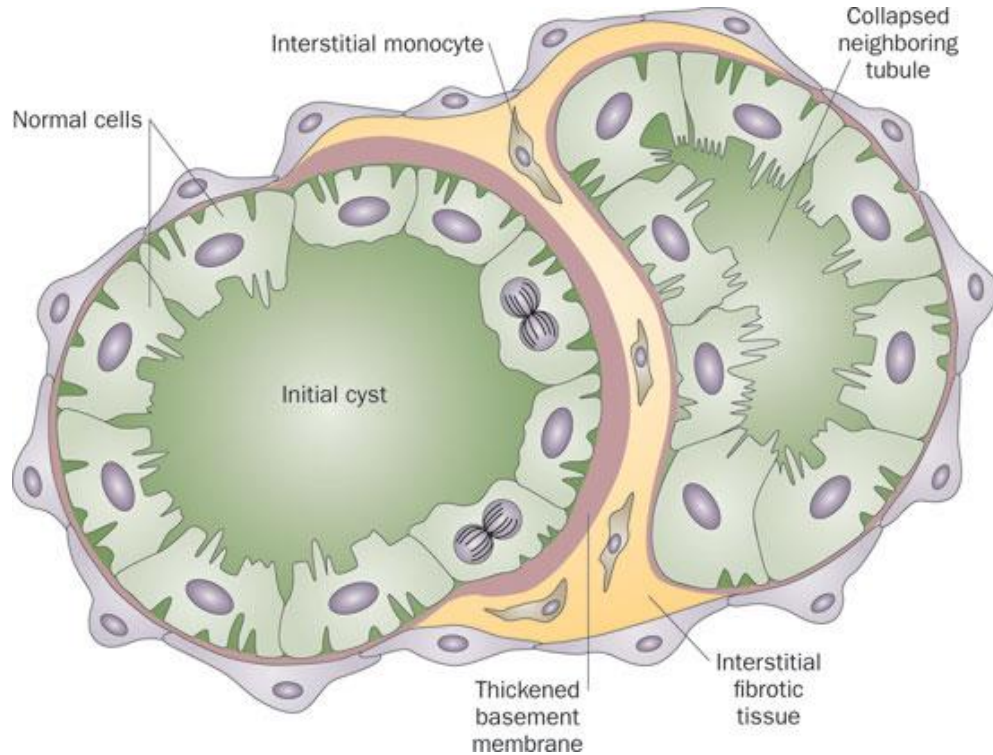


Figure 1.1: Illustration of the early stages of cyst formation and enlargement with fibrotic tissue deposition.

normal tubule geometry. However, in addition to this other unidentified factors promote the proliferation of cells that give rise to fluid-filled saccular cysts. These are benign tumors that directly invade and displace adjacent parenchyma. As these cysts begin to emerge the extracellular matrix is also modified causing an expanding mass (Figure 1.1). An inflammatory response then takes place with the proliferation of macrophages; these along with resident fibroblasts cause fibrosis as a response to potential perceived injury[25].

The cysts detach from the tubules when they grow greater than 2 mm and become isolated sacs filled with trans-epithelial secretions. These apply pressure on normal tubules and further induce an inflammatory response leading to extensive

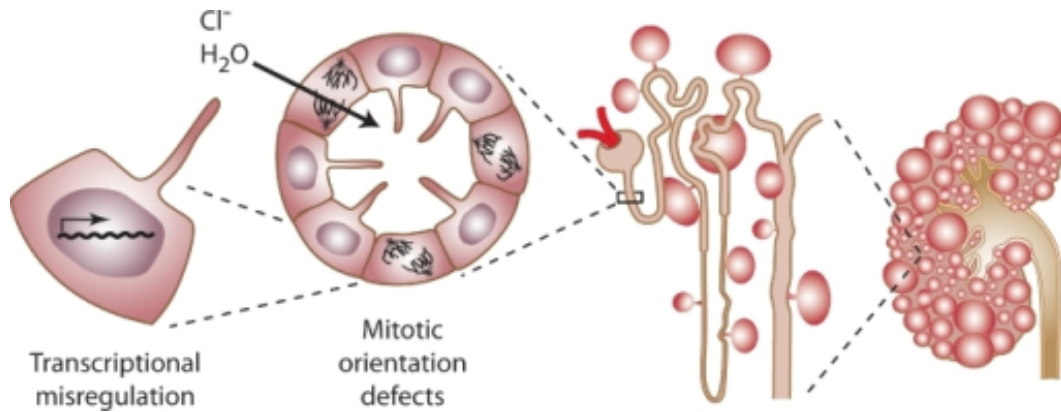


Figure 1.2: Cyst formation at the level of the cell, nephron, and kidney. Defects in the genes encoding PKD1 or PKD2 lead to aberrant gene transcription, cell proliferation, and ion secretion, which in turn result in the formation of fluid-filled cysts. As cysts balloon out from individual nephrons, their collective effect leads to the displacement of the normal renal parenchyma and the formation of a cyst-filled kidney with reduced functional capacity. Cyst formation at the level of the cell, nephron, and kidney. Defects in the genes encoding PKD1 or PKD2 lead to aberrant gene transcription, cell proliferation, and ion secretion, which in turn result in the formation of fluid-filled cysts. As cysts balloon out from individual nephrons, their collective effect leads to the displacement of the normal renal parenchyma and the formation of a cyst-filled kidney with reduced functional capacity.

fibrosis. The vasculature around these cysts is obstructed thereby affecting glomerular function and in turn limiting the kidney's normal capacity for proper filtering. This cycle of injury response is repeated endlessly (Figure 1.1). Nephrons are destroyed and replaced by cysts that are supported by fibrotic tissue causing a severe reduction in the functional parenchyma[7].

1.1.1 Screening and diagnosis of ADPKD

Many patients without a hereditary history of the disease are typically asymptomatic and ADPKD diagnosis takes place when the patient displays symptoms such as hypertension, sudden onset of renal pain, and haematuria. Around half of ADPKD patients aged 20-34 display hypertension and a normal renal function. Abnormal re-

modeling of renal parenchyma, reduced blood flow, increased filtration fraction and abnormal renal handling of sodium are identified as contributing factors[56, 57, 54]. Renal pain is contributed by the abnormal endothelial growth associated with cystogenesis which can promote hemorrhage and gross haematuria. Patients can develop flank pain which can be associated with the passing of kidney stones. Around 20% of patients have kidney stones. ADPKD patients are also susceptible to urinary tract infections[54]. In addition to the presence of cysts in the kidney, they are also found in the liver, pancreas and the intestines. Patients are also at an increased risk of suffering from further complications such as aortic aneurysms, heart valve defects and in rare cases intra-cerebral aneurysms.

Typically, establishing a diagnosis of ADPKD in patients presenting above mentioned symptoms is straight forward. In some cases however, cystic development in kidneys can be a result of hereditary and acquired disorders that are not ADPKD. Patients exhibiting autosomal dominant polycystic liver disease(PCLD) is often misdiagnosed for a mild form of ADPKD. These patients can sometimes present with a few renal cysts, but they don't develop end stage renal disease[48, 29]. ADPKD can also be confused with autosomal recessive polycystic kidney disease (ARPKD) due to the onset of the disease in adulthood. Mutations in the uromodulin gene, encoding the Tamm-Horsfall protein, on chromosome 16 can cause the autosomal dominant medullary cystic kidney disease(MCKD)[28]. It is symptomatic in the adulthood with renal dysfunction and occasional renal cysts which may be confused with ADPKD. Although ADPKD is a hereditary disease, several studies have suggested that a significant portion of the patients lack a family history. This could either be attributed to the presence of a *de novo* mutation, estimated to be present in less than 10% of the cases, or a failure to diagnose the disease in mildly affected family members[49].

Ultrasound is the first choice imaging modality for diagnosing at risk patients

for ADPKD. Ravine et al. found an age stratified ultrasound criteria for ADPKD which was later corroborated by Pei et al. The recommended criteria are as follows. For individuals at risk in age group 15 to 39 years it is the presence of "Three or more unilateral or bilateral renal cysts". This showed a positive predictive value of 100% and a sensitivity of 81.7% for age group 15-29 and of 95.5% for age group 30-39. A PPV of 100% and sensitivity of 90% was associated with age group 40-59 when the criteria was "At least two cysts in each kidney". For the age group of 60 and above, "Presence of at least four cysts in each kidney" had a PPV and sensitivity of 100%.

1.1.2 Management of ADPKD

Currently there are no therapies to prevent ADPKD patients from developing ESRD due to loss of parenchyma due to cystic burden. However, advances in understanding of genetic and molecular pathways of the disease has spurred several clinical trials for therapies to reduce the rate of cyst growth and slow down the progression of ADPKD. Myint et al.[39] did a meta analysis of all the clinical trials that were aimed at testing therapies to reduce the cystic growth. They found that for a period of 18-24 months, treatment with Target of Rapamycin Complex 1 (TORC1) inhibitors did not alter the progression of TKV. A rate reduction of up to 9% in TKV was observed with treatment using somatostatin analogues but no effect on GFR progression was noted. A 36 month long treatment with tolvaptan reduced the annual rate of TKV increase by 2.5% when compared to the placebo group and also noted an improvement in GFR decline[53]. Apart from these findings, treatment for ADPKD involves mitigating symptoms discussed in the previous section.

1.1.3 Prognostic biomarkers to monitor disease progression

In a chronic kidney disease (CKD), functional measurement is done in terms of the glomerular filtration rate (GFR) as the disease has a direct effect on the ability of the glomeruli to generate filtrate. In clinical practice, the National Kidney Foundation's Kidney Disease Quality and Outcome Initiative (NKF-K/DQOI) define chronic kidney disease as a GFR of less than 60 mL/min per 1.73 m², regardless of the cause[6].

GFR is considered a fundamental indicator for disease progression in most escalating renal disorders. However, it can be highly misleading in the case of monitoring kidney efficacy in ADPKD patients. Kidneys have a remarkable ability to compensate for the loss of filtration ability. The patchy distribution of cysts and the associated loss of healthy parenchyma leaves behind islands of functional areas that typically escape any injury from inflammation, scarring, and apoptosis caused directly or indirectly by cystogenesis. These islands are responsible for remarkable hyperfiltration and compensation to offset the lost GFR[61]. As a result of this, in ADPKD patients, the GFR is maintained in normal range until about the fourth or the fifth decade of life. Eventually, these functional areas are lost after years of service and the GFR begins to fall drastically. As a result, GFR is a very insensitive measure of renal function in ADPKD to monitor disease progression before it is significantly compromised. Woon et al.[62], have conducted an in-depth review of the various published work on prognostic markers for disease progression in ADPKD. However, it has emerged that there is a lack of unanimous agreement in the community about the factors for prediction of renal outcomes and the variables that need to be measured to predict and monitor disease progression, total kidney volume (TKV) seems to be a strong surrogate biomarker that can be used to predict declining renal health. TKV

is defined as the sum of the volume of the left and right kidney.

The Consortium for Radiologic Imaging Studies of Polycystic Kidney Disease (CRISP) was established to study the progression of disease in early stage individuals. CRISP has created a resource of MRI data, renal function parameters and other selected markers (genetic, molecular) in correlation to disease progression. This research thrust has revealed that kidney volume measurements from MRI can be considered as the gold standard for assessing the yearly progression of the disease[26]. The decline in renal function, which eventually leads to ESRD, is strongly associated with the enlargement of the kidney, which is in turn driven by the expansion in number and volume of cysts in the organ. CRISP and various other groups have conducted studies that have shown a significant relationship between total kidney volume (TKV) and kidney function[14]. Having been considered the best representative marker in predicting declining renal volume[45], kidney volume growth needs to be accurately monitored over a short period of time in order to assess the efficacy of new therapeutic techniques. Research has shown that early intervention in ADPKD promises more therapeutic benefit than late treatment, as cysts have not yet replaced the bulk of intact renal parenchyma and renal function is still maintained[53, 52]. These novel, and often experimental, therapies are aimed at controlling the rate of cystic development as a specific treatment for ADPKD. Other than supportive care treatment does not exist.

1.1.4 Imaging for prognosis

In current practice MR and CT imaging are used to monitor the rate of kidney volume enlargement. CRISP has developed reliable MR-based protocols to measure and detect relatively small changes in TKV over a small period of time in ADPKD

patients[4, 55]. The volume of individual kidneys is measured from tomographic images using stereology method, which has been widely used to measure volumes of a variety of organs. In this technique, the measurement is done by counting the number of intersections of a randomly oriented and positioned grid over the region of interest. The area of this region is calculated and the total volume is obtained by summing the products of area measurement and the tomographic slice thickness essentially voxel counting method. MR is used over CT because it provides high-resolution 3D images with excellent tissue contrast without the exposure to ionizing radiation or iodinated contrast agent. A multi-center study has shown MR imaging to be well suited to assess kidney morphology and changes in renal volume[4, 16]. The use of gadolinium contrast media further enhances the ability of MR for this application, however, previously held belief about the relative safety of gadolinium for renal imaging has changed. New research has indicated that for patients with impaired renal function, the clinical benefits and risks of using MR contrast need to be considered carefully. This is especially a concern when imaging ADPKD patients. In addition to this, MR imaging involves relatively long image acquisition times and image quality varies with different scanners.

Ultrasonography (US) is a great technique for performing diagnostic as well as interventional imaging. Ultrasound has advantages that it is a non-ionizing, real-time and multi-planar method that can be utilized at the bedside. It also has fast scan times and is incredibly cheap, both in terms of capital investment and long term use, when compared to MR scanning systems. These characteristics make US a great candidate for diagnosis of ADPKD and long-term monitoring of disease progression. However, studies have indicated that this technique is inconsistent for short term analysis of kidney volume. A study conducted to compare the efficacy of US versus MR for volume measurement showed that using current standard protocols, US show

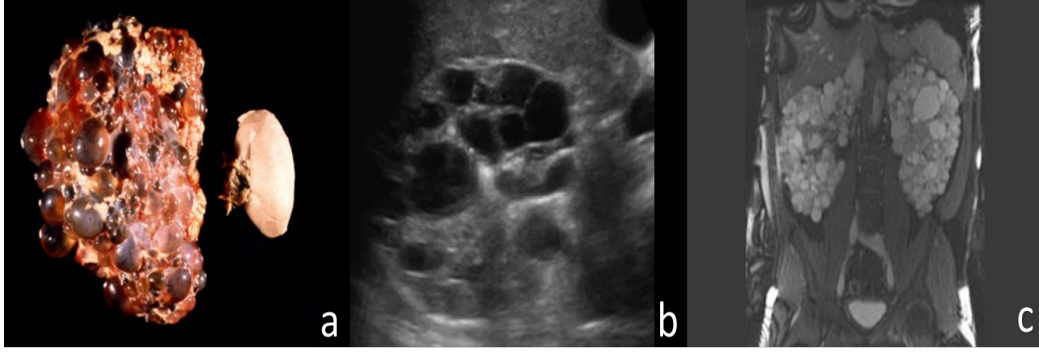


Figure 1.3: Autosomal Dominant Polycystic Kidney (a) as compared to a healthy kidney, (b) imaged under ultrasound and (c) imaged under MRI.

a substantial systemic underestimation to the tune of 25% of renal volume when compared to MR measuring techniques[5]. This indicates the limited accuracy of US for precise measurements of TKV. In addition to this, it has been shown that the repeatability of this method is not very good. For inter-observer variation in US renal volumetry, it was observed that the standard deviation spread anywhere from 16% - 48% of the TKV as compared to MR techniques where the variation was in a range of 2% - 3%. However, the correlation between US and MRI volume was shown to be 0.88 - 0.89[44]. This is a very good indicator that US needs to be further explored as a viable modality for precise and reproducible measurement of TKV in ADPKD patients.

1.2 Specific Aims

Aim 1: Development of a tracked ultrasound system.

In this aim, our goal is to build a system that is capable of augmenting 2D ultrasound imaging with spatial tracking data. Doing so enables us to localize real-time imaging information within the physical framework of patient anatomy. Tracked

ultrasound also gives us the ability to generate 3D datasets of regions of interest dynamically, thereby furnishing with the latest changes to tissue or structures under the scanning plane of the probe. We will implement state of the art calibration techniques to minimize localization errors between the ultrasound images and patient anatomy.

Aim 2: Use statistical shape analysis of kidneys to develop techniques for accurately measuring total kidney volume (TKV).

The goal of this aim is to generate shape models of kidneys in order to capture the variation in volume within a population. We will treat the shapes as a Gaussian mixture model and generate mean shape and capture majority of the variation within 3SD. We believe that by doing so, we can also capture the variation in total kidney volume accurately. Once the model is generated, tracked ultrasound developed at the end of aim 1 will be used to capture a kidney volume of the patient in question. The captured volume will then be registered with the shape model using deformable coherent points drift (CPD) algorithm. The rationale behind this is to use the shape information from the US and use this to drive the change in shape model, which will accurately predict TKV.

Aim 3: Perform mock clinical experiments using tissue analogous phantoms to assess the efficacy of developed techniques.

We will quantitatively test our techniques within clinically acceptable margins through a set of mock clinical experiments. We will construct a series of tissue analogous phantoms. The phantoms will then be subjected to tracked ultrasound imaging to generate a volumetric scan. The US volume will be registered with the statistical shape model and TKV will be calculated using techniques developed in Aim 2. The computed values from ultrasound images will then be compared with the CT volume to assess the quantitative efficacy of our method.

Chapter 2

Development of a tracked freehand ultrasound system

2.1 Introduction

2.1.1 Image-guided surgery (IGS) paradigm

Over the past decade, development of hardware for positional tracking of tools has allowed for interactive approaches to imaging and therapy guidance[17]. A tool within the procedure room is tracked using a positional localizer within an arbitrary coordinate system (physical space or tracker space). Tracker space is co-registered with pre-operative medical images and/or the intra-operative imaging system (image space). With co-registration, the location of surgical tools can be reported relative to the position in the medical images. These techniques are analogous to using GPS navigation when applied to the human body. Subsequently, they are employed for (i) procedure planning (planning intervention based on diagnostic and pre-procedure images), (ii) intraprocedural targeting (for guidance of tool, e.g. Needle, to the in-

tended target), (iii) intraprocedural monitoring and control (monitor tissue changes make adjustments), and (iv) post-procedural assessment (assess and monitor efficacy of procedure).

At the heart of any image-guidance system is spatial tracking. The role of a tracking system is to determine the position and the pose (orientation) of the sensor, which is attached to the medical instrument, and as an extension of the medical instrument is within its frame of reference. In the IGS domain, there are typically four technologies that exist to spatially localize medical instruments: 1. Mechanical 2. Acoustic 3. Electromagnetic and 4. Optical (Figure 2.1).

Mechanical Tracking

Mechanical tracking systems consist of articulated arms where the tip position is determined by inverse kinematics. Mechanical arms are accurate, however can only track one object at a time and are quite cumbersome. FARO surgical arm (FARO Medical Technologies, Orlando, FL) is a mechanical tracking system used in practice.

Acoustic Tracking

These tracking systems compose of emitters (speakers) and receivers (microphones) that work in ultrasound frequency range. The position of the receivers is computed using two approaches: 1. Time of Flight measurement of the propagation time of sound waves between the emitters and receivers and 2. The phase difference between the sound waves emitted and received. These systems are sensitive to variations in temperature, pressure and humidity which affect the speed of sound in air. They also require constant line of sight and an area free of any ultrasound source.

Electromagnetic Tracking

The idea for magnetic tracking has been around since the 1970s when Wynn et al. presented a method for sensor localization in 2D[63]. The idea behind magnetic tracking is in measuring the currents induced in receiver coil placed in the medical

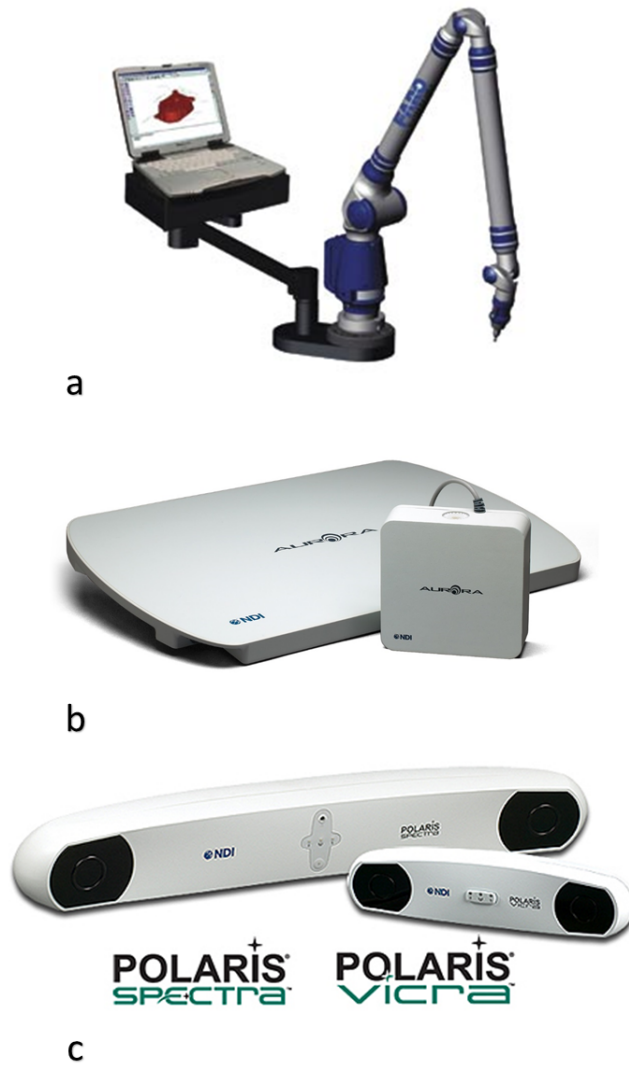


Figure 2.1: Mechanical tracking system FARO arm (a), Electromagnetic tracking system NDI Aurora (b), Optical tracking system NDI Polaris and Vicra.

instrument when moved in a magnetic field. The field can be generated by either alternating current (AC) or direct current (DC). EM tracking uses the known geometry of the magnetic field to determine the position and orientation of sensors used to measure the magnetic flux. The geometry of the field is governed by the Biot-Savart law and controlling the coil geometry can set determine the shape of the magnetic field. Special sensors are then used to measure the magnetic flux inside this field to back out the spatial position and orientation with respect to the field geometry[64, 22]. Electromagnetic tracking is susceptible to two metal related phenomenon that are present in the operating or clinical environment: ferromagnetism and eddy currents. Ferromagnetism affects both AC and DC tracking as it influences the geometry of the field generated. AC systems are at a risk of field distortion due to the generation of eddy currents that can be generated in metallic objects in its field vicinity. Under ideal conditions, electromagnetic tracking systems are capable of error rates ranging from 0.5 mm to 1.5 mm depending up on their application and surroundings of use[31].

Optical Tracking

Optical tracking involves use of multiple cameras with distributed markers affixed to a predefined rigid geometrical structure. A minimum of three markers are required to determine the pose of the rigid body. Optical tracking systems can be divided into three categories: 1. Videometric systems, 2. Infrared based tracking systems and 3. Laser tracking systems. Videometric systems involve multiple calibrated cameras that identify marker patterns on image sequences. Well known commercial system is the Claron tracker (Claron Technology Inc., Toronto, Ontario, Canada). IR based systems use an optical filter to eliminate all wavelengths of light except IR. These systems employ active IR markers or passive markers. Active systems use IR LEDs that are sequentially fired and detected by either planar or linear charged

coupled device (CCD) units. Using the process of triangulation based on the sequence of firing and known geometric configuration as well as the distance between the CCD elements, the pose of the rigid body is estimated. In passive systems, IR reflective spheres arranged in a predefined unique geometry are used. The camera system employs 2 CCDs and the pattern of the reflective markers is identified on a 2D image. The pose is determined using stereo geometry. In laser tracking systems an array of photo-sensors are mounted on a rigid body with predefined geometry. A semiconductor laser emits light that is reflected by rotating mirrors into 2 or 3 fans of coherent lasers. The volume is swept by a fan shaped laser beam and the position of the rigid body is estimated by simultaneously sampling the position of the swept fan and the signal from the photo-sensor[13]. The most popular optical tracking in use are the IR-based systems and the success of these in the clinic is owed to its high accuracy. Localization accuracy for the Polaris Spectra is about 0.25 mm to 0.3 mm in its standard and extended pyramid zones[60, 19]. The Polaris Spectra showed a tracking error of 0.33 mm in active mode and 0.64 mm in passive mode.

For this work, we chose to use the Polaris Spectra system in active tracking mode.

2.1.2 Tracked freehand ultrasound

Since the discovery of X-rays in 1895 by Wilhelm Roentgen, medical imaging has been used to visualize the interior structures in human body in two-dimensions. As indispensable as 2D imaging is, most information about human anatomy is lost to the physician owing to the 3D structure of internal organs. Diagnostic imaging has seen a massive boost in visualizing 3D anatomical information with the advent of CT and MRI technologies. Ultrasound is conventionally a 2D modality. It is used

to capture a series of 2D images that the operator interprets mentally to form a subjective impression of the 3D anatomy. The skill and experience of the user plays a big goal in the diagnostic or interventional accuracy.

The limitation is in the fact that the user has to mentally transform a large number of 2D images to form a 3D impression of the internal structure and its associated pathology. This is highly variable and subjective and can cause disagreements in diagnosis, planning, and delivery of therapy effectively. Staging and planning of procedures also often requires accurate anatomical dimensions. The issue with 2D ultrasound is that techniques to calculate the volume of tumors or organs is often done from their linear measurements such as height, length, and width using estimation formulas based on the 2D view. This can cause low accuracy and high variability due to operator dependence. 2D ultrasound, being a real-time modality is still suboptimal to monitor therapeutic procedures effectively. The operator has to constantly adjust the 2D plane of viewing to keep the same anatomical site in the field of view where the therapy is being delivered. This requires a long learning curve and a lot of experience. 3D ultrasound is a modality that can ameliorate some of these issues.

Typically, 3D ultrasound is generated from combining a stack of 2D slices around an anatomical region of interest. Unlike CT and MRI, images can be generated in arbitrary orientations and at a high rate of acquisition. This results in unique challenges and opportunities to extend 2D ultrasound to a 3D imaging modality. There are typically four methods to acquire 3D ultrasound:

1. *Constrained sweeping systems* are mechanical systems that sweep the entire probe over a predefined area. The slice acquisition is either in a wedge pattern, parallel or rotation around a central axis. Typically an external motorized rig is used to control the sweeps of the probe.

Table 2.1: Summary of 3D scanning methods, acquisition modes and disadvantages.

<i>Scanning method</i>	<i>Image acquisition method</i>	<i>Disadvantage</i>
Constrained sweeping systems		
Linear Tilt Rotational	Acquired images are parallel to each other with equal spacing; images are fan-like with equal angular spacing; images are propeller-like with equal angular spacing	Bulky device; resolution degrades with depth; motion related artifacts
Untracked freehand systems		
Image correlation	Measure speckle decorrelation between adjacent images	Special computing required; compound motion is difficult to track
Tracked freehand systems		
Magnetic sensor Optical sensor Articulating arm	Slice positional data is obtained from magnetic field generated, optical triangulation or angulation between joints in moving arm	magnetic systems prone to errors in presence of field distorting materials; optical systems need line of sight; mechanical arms are too bulky and cumbersome
3D probes	2D phased array transmits a diverging pyramidal beam and returned echoes are displayed in real time as multiple planes	System cost and signal/noise

2. *3D ultrasound probes* use 2D arrays of ultrasound crystals inside the probe housing. The crystal arrays are either mechanically steered or are controlled via electronic beam steering. These probes are usually larger and more expensive, but suffer with lower quality image resolution as compared to 2D probes[51, 34]. In some probes a ring like probe can be accurately controlled by an internal motor to acquire high resolution 3D volumes.
3. *Sensor-less techniques* use information from 2D images to align it with temporal data to generate 3D volumes. Decorrelation or linear regression is utilized to analyze the speckle in US images to align the volume[59, 47].
4. *Freehand systems* typically consist of a sensor attached to a the ultrasound probe which is tracked by a spatial localization system in 3D space. The clinicians scan the area of interest and along with the images, the trajectory, position and orientation data is recorded. Subsequently, this information is used to calculate the location of each pixel in the image in physical (3D) space. These pixels, and as an extension the imaging data, are now located within a frame of reference. This allows for various ways the data can be used. One example is being able to co-register the ultrasound data with other modalities. Before the data from the images can be used, the rotational, translation and scaling information needs to be computed via calibration schemes.

In this work we are using the tracked freehand system and the following sections will describe the methods utilized to implement such a system.

2.1.3 PLUS Toolkit

For our work, we utilize the tools provided in the open-source PLUS toolkit [33]. PLUS is a freely available, simple to use toolkit for the rapid prototyping of clin-

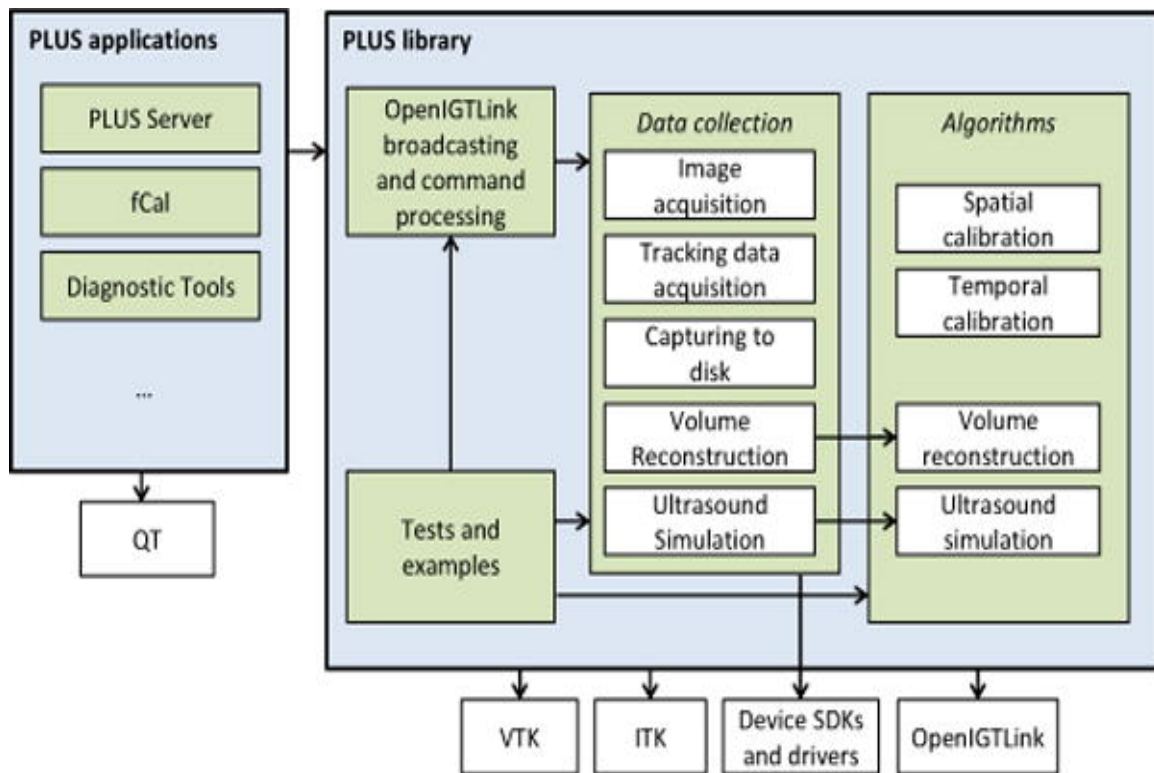


Figure 2.2: Software components of PLUS toolkit[33].

ical research work-flows that are based on tracked freehand ultrasound. The toolkit consists of the core library and applications built using the functionality encapsulated in the library. The goal is to provide a hardware independent interface to obtain image, pose and time information to implement ultrasound based guidance work-flows. To maintain interoperability PLUS uses standardized data representation.

Image Data

In ultrasound based work-flows, image orientation plays a crucial part and needs to be defined for every ultrasound slice. It represents the relationship between the physical transducer axes and the image slice axes. In PLUS this is defined by a two letter acronym that represents the transducer orientation with respect to the image axes in the +x and +y directions. The four directions are defined as: Marked(M) - Direction towards the marker on the probe, Unmarked(U) - Direction away from the marker on the probe, Far(F) - Direction facing away from the transducer face, and Near(N) - Direction going into the transducer face[33].

Pose Data

In PLUS a frame of reference is specified to define the pose of images, and tools for each individual item and the transformation between them. A 4x4 homogeneous transformation matrix represents this and each coordinate system is defined by its name, origin position, axis direction and scaling units. In addition to this, the process of computing transformation between two arbitrary reference frames is required. For this PLUS stores all the transforms as edges of a graph, where each vertex represents a coordinate system.

All transforms in PLUS are stored in a transform repository that is accessible throughout the entire framework. Each transform is uniquely identified by its name. PLUS uses a standard naming convention. The transform name is constructed from the name of the reference frames that it transforms from to the name of the reference

frame it transforms to, with the word "To" in between[33].

The transforms are computed automatically. As mentioned above, all the transformations and their inverses are stored in a system-wide directed graph. Each vertex is identified by the coordinate system name it represents. To compute the transformation, first the path (series of transformations) between two vertices (coordinate systems) is identified and then the corresponding transformation matrices are multiplied and inverted as needed. The goal of having one repository is to avoid ambiguity in the definition of transformation names[33].

Time Data

PLUS also implements methods to time-stamp data-items. It uses a system time internally for all time stamps. The system time is obtained from a high-resolution on-board timer and starts at 0 when any PLUS application is launched. PLUS converts all the hardware device timestamps to system time-stamp.

In PLUS ultrasound and tracking data are independently acquired from different hardware. It is therefore required that these data streams be fused together. In order to handle this, in PLUS, each hardware device or processing algorithm is treated as a "Device". The device receives and provides data through "Input" or "Output Channels" and can either generate data internally or receive data from another device via the other device's output channel. Each hardware device has a corresponding device in the processing pipeline in PLUS. In addition there are "Virtual Devices" which perform operations such as fusion of multiple channels, disk storage, volume reconstruction, or simulated data generation. The channels store data in a circular buffer to allow for temporal calibration and mitigate any data loss issues. In addition, PLUS needs to resample data before fusion as data is acquired at different time points. As resampling image data is complex, PLUS resamples the pose data at each time point during image acquisition before data fusion[33].



Figure 2.3: Sonosite M-Turbo with 6-15MHz linear array probe.

In PLUS all the definitions of hardware configurations, acquisition and connection related settings, device and virtual device configurations are stored in an .xml based configuration file[33].

2.2 Methods

2.2.1 Construction of tracked ultrasound probe

The ultrasound system in use is the portable Sonosite M-Turbo (Fujifilm SonoSite Inc., Bothell, Washington) with a 6-15MHz linear array probe (Figure 2.3). The probe is mounted with an actively tracked rigid body marker. For our application we use the Polaris Spectra system with active IR based tracking. The rigid body marker is constructed using the wiring diagram described in Figure 2.4 according to which IR LED's are populated on the marker surface. Individual LEDs are turned on when appropriate rows and columns are energized. The optimal way to wire LEDs is

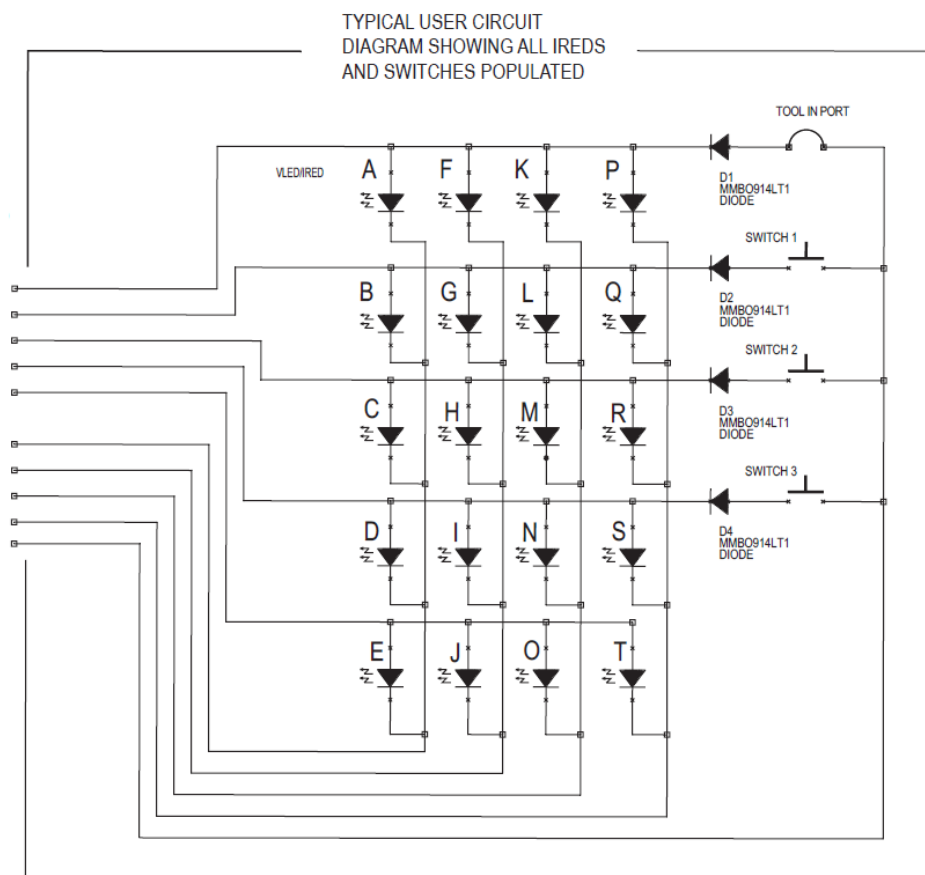


Figure 2.4: Polaris active tool marker wiring matrix.

to distribute them evenly across the columns so as to fire them at equal intensities. In our tools, the LEDs are positioned in locations A, G, M ,and S. Each active marker contains a serial read only memory (SRAM) device that stores the tool definition file. The tool definition file is generated as a result of tool characterization. The tool definition file stores information containing the geometry of the tool, the manufacturing data, settings and parameters, and the wiring definition.

2.2.2 Calibration of tracked ultrasound probe

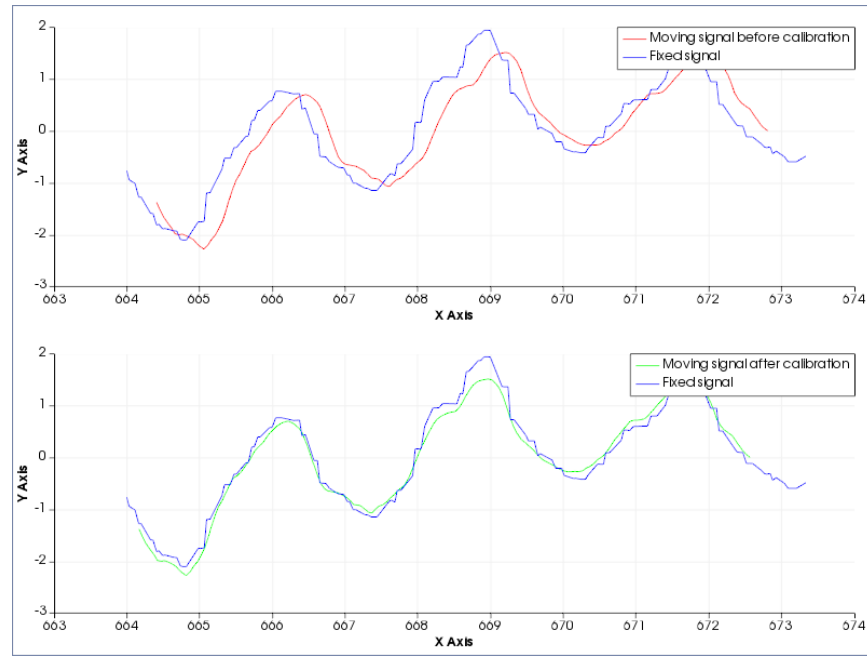


Figure 2.5: Plot of temporal offset for calibration at imaging depth of 6 cms before and after applying offset. The moving signal represents tracker pose data and fixed signal represents imaging data.

Temporal Calibration

The tracked ultrasound systems in research setting, as in our case, often consist

of dedicated hardware for image acquisition and processing, for acquiring pose data and the US system. These systems typically timestamp their data using their internal clocks. Occasionally some devices also do not provide with a timestamp for their data stream. In order to accurately track images and relate them to the appropriate pose data, synchronization via correct timestamps is vital. In order to do so a temporal calibration scheme needs to be carried out.

To carry out temporal calibration, the tracked probe is moved along the vertical axis in a tank filled with water. The key is to image the bottom of the tank while moving the probe in a quasi-periodic motion. The position signal for tracker is calculated as the position along the principle axis of motion. For the image data the bottom of the tank is taken as the feature of interest and its change in position along the vertical axis is noted. The time offset is then calculated from the two positional signals where the highest correlation between the two signals is obtained.

Spatial Calibration

Ultrasound is a real-time imaging modality and its data is rapidly changing in time. In contrast tomographic modalities like MRI and CT have static and well defined data. Because of this rapidly varying nature of US data, it is vital to establish a common frame of reference for this data in the context of an image-guidance system. The positional tracking marker attached to the ultrasound probe, let us call it sensor, returns the 3D location of itself rather than the ultrasound image plane. This position is in the tracker space or the world coordinate system. The goal is to find the relative location of the imaging data in 3D space and therefore to obtain the pose of the image in terms of the world coordinate system. The process of finding the transformation from image pixels to sensor ($T_{S \leftarrow I}$) involves determining six parameters- three translations and three rotations[30].

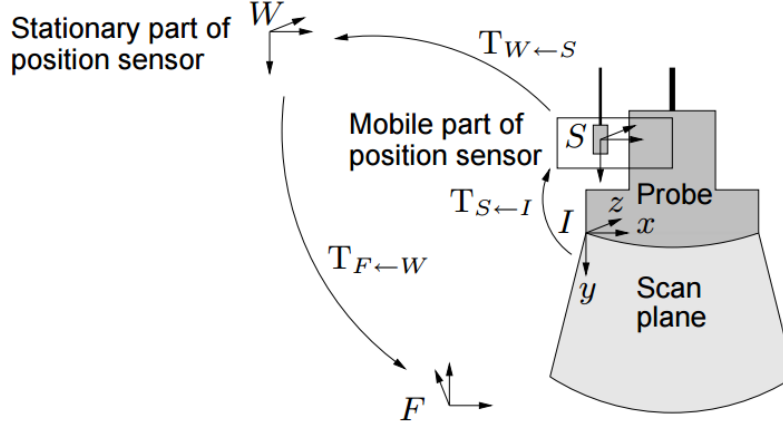


Figure 2.6: Illustration of coordinate system and transforms involved in a freehand ultrasound system[30].

Figure 2.6 illustrates the transformations involved in calculating the 3D location of a point from the image plane (scan plane). $T_{S \leftarrow I}$ is the transformation that needs to be calculated via the process of spatial calibration. $T_{W \leftarrow S}$ is the transformation describing the sensor with respect to world coordinate frame and is obtained from the tracking information given by the pose tracker. $T_{F \leftarrow W}$ is the transform between a the world coordinate frame to the calibration phantom. The location of point in 3D space is then given by[30],

$$P = T_{F \leftarrow W} T_{W \leftarrow S} T_{S \leftarrow I} S P_{image} \quad (2.1)$$

where S is the scale in the image plane.

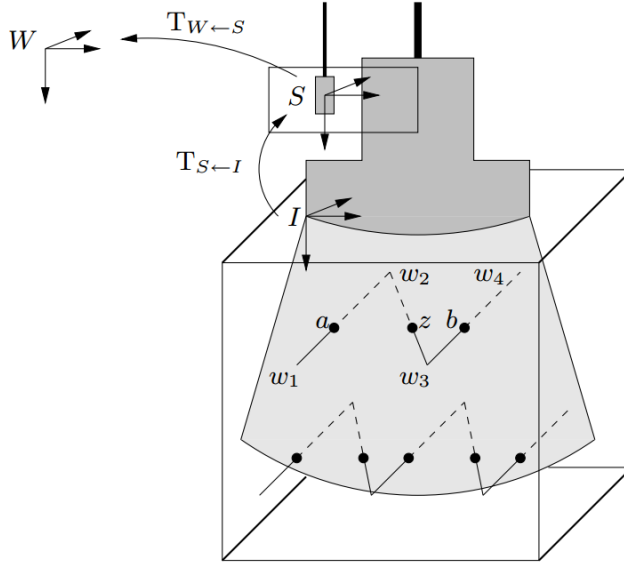


Figure 2.7: Illustration of Z-wire phantom used in freehand ultrasound calibration[30].

The phantom used in this case is called the Z-wire or the N-wire phantom. In this type of phantom wires are arranged in a 'Z' or 'N' shaped configuration (Figure 2.7) and the phantom is precision manufactured. This is done in order to accurately know the geometric locations of the wires in 3D space. The phantom typically has divots which are the points of reference from where the location of the wires is precisely known. The phantom is then registered to the tracker (world coordinates) using a calibrated stylus which is used to locate the divots on the phantom in physical space. The location of the the tip of the stylus is known with respect to the tracker and as a consequence after registration, the location of the wires is also known in 3D space via the transform $T_{F \leftarrow W}$.

As illustrated in Figure 2.7 the absolute positions of w_1, w_2, w_3 and w_4 are known. In order to find the transform needed, first the location of point z needs to be determined in 3D space. To do this the wires are scanned under water using

the probe. The wires appear as points in the image plane and are segmented. This gives the distances $|z - b|$ and $|a - b|$. Due to similar triangles, the ratios of these quantities remain the same in the image plane as in the real world. Using this, point z is determined as,

$$z_{world} = w_3 + \frac{|z_{image} - b|}{|a - b|}(w_2 - w_3) \quad (2.2)$$

The transformation $T_{S \leftarrow I}$ can then be found by minimizing the following function[30],

$$f = \sum_{i=1}^N \sum_{j=1}^M |T_{W \leftarrow S}^{-1} z_{ij(world)} - T_{S \leftarrow I} S z_{ij(image)}| \quad (2.3)$$

where N are the number of images of the phantom captured and individual images containing M number of z-fiducial points. The implementation provided in PLUS is as described by Carbajal et. al[12].

2.2.3 Volume reconstruction of tracked images

In order to generate the volume, each pixel from the 2D image needs to be placed into a 3D volume corresponding to its real world location given by the transformations given via the pose information. In PLUS this is done either via placing the pixel information into a corresponding voxel by nearest neighbor interpolation or it is distributed among 8 voxels via linear interpolation. The value of the pixel to be inserted is averaged between overlapping 2D slices for the same location if more than one pixel have the same pose information.

In tracked ultrasound, the stacks of 2D slices are bound to have uneven slice spacing and orientation. Due to this when putting together a 3D volume, artifacts due this misalignment can manifest itself as regions of unfilled data. These regions need to be filled to have a consistent volume. In order to do this, in PLUS, a 'hole'

filling method is implemented. This is done by interpolating the voxel values based on nearby known voxels using a gaussian or an elliptical kernel[33].

2.2.4 Evaluation of calibration

In order to evaluate the accuracy of calibration, two objects of known dimensions were scanned and their volume was reconstructed. The two tests used to check for accuracy were to measure the distance accuracy and the volume accuracy.

For distance accuracy measurement the edge of a cuboid of known dimensions was scanned. The goal was to reconstruct this edge in 3D to get distance measurement between the endpoints of the line segment that the edge represents. The error is then measured as,

$$Error_{distance} = |Distance_{world}(P_1, P_2)| - |Distance_{3D}(P_1, P_2)| \quad (2.4)$$

The object was scanned in a manner where the probe was made to do a tilt sweep rather than parallel sweep of the edge as this prevents an uniform offset of error to be applied due to bad calibration[30]. By scanning the object in a tilted sweep in different directions the error is applied non uniformly to the reconstruction, which is desirable as a uniformly applied error generates higher accuracy results which are misleading.

In our application volumetric measurements are of importance and assessing the accuracy of this task gives us a better metric. Again, two objects, one a cuboid and a cylinder of known dimensions, are scanned using tilt sweeping techniques. The volume is reconstructed in 3D space and the difference in the volume between the real world volume and the reconstructed volume is the error metric.

Table 2.2: Actual and measured dimensions of cuboid using tracked ultrasound

	Actual	Measured	Error
Length (mm)	100	102	2
Width (mm)	38	39	1
Volume (mL)	144.4	155.1	10.7

Table 2.3: Actual and measured dimensions of cylinder using tracked ultrasound

	Actual	Measured	Error
Length (mm)	100	106	6
Diameter (mm)	22	20	2
Volume (mL)	38.02	33.30	4.72

2.3 Summary

With the availability of spatial localizer technology, it is possible to track and accurately obtain pose information about tools that are used in a clinical environment. This has enabled development of new clinical workflows that utilize the precise positional information of tools to plan and guide therapy. For our work, we have utilized Polaris optical tracking in order to track 2D ultrasound frames in 3D physical space in order to generate 3D volumetric data of a region of interest which is subjected to some form of therapy or analysis. In our work, the goal is to utilize tracked 2D ultrasound to recover 3D shape information for the kidney in order to calculate the volume of the organ. For this a tracked ultrasound probe was constructed that used active tracking and a tracked ultrasound system was implemented using the PLUS toolkit. In order to acquire accurate volumetric data, the system was subjected to steps of calibration. Since the entire system is loosely coupled of components which

comprises of tracking system, ultrasound interfaced to a PC via a frame grabber and the processing software on the PC at first, a temporal calibration scheme was performed. The goal of this was to make sure all the data streams were in sync and the pose information acquired from the tracking system accurately corresponded with the image information gathered from the ultrasound system via the frame grabber. Following this, a spatial calibration was performed. Spatial calibration is a vital step as it is important to obtain the position of a feature of interest in the image plane in terms of its real world coordinates. In the system implemented here, we used a linear array with frequency from 6-15 MHz that was calibrated for an imaging depth of 6 cms. The accuracy was then verified by scanning objects of known dimensions and was found to be within a few millimeters, which is reasonable for our application.

Chapter 3

Development of statistical shape model of the human kidney

3.1 Introduction

The shape of an object can be mathematically represented as a set of n points in any dimension (typically 2D or 3D for our application). The configuration of points in a shape is of the highest quality when it is invariant under some transformation. This configuration does not change when the shape is translated, rotated or scaled (similarity transform). The statistics of shape allow us to analyze shape differences and changes by applying formal statistical techniques. The goal is to seek a parametrized model of the form, $x = M(b)$ where b is a vector of parameters of the model. This model can then be used to generate other new vectors based on b .

Principal component analysis (PCA) is a statistical method that applies an orthogonal transformation to convert a collection of observations with possible correlation to a set of linearly uncorrelated variables called principal components. Each principal component is used to measure the variance in data along one of a set of

orthogonal directions in the space of measurements. The first component describes the largest variance in the data, with the subsequent ones having lesser influence.

In PCA based shape models, the variation in shape is learned from a set of training shapes X_1, \dots, X_n . Each shape is made up of discrete landmark points. These can range from a few points of interests taken at certain anatomical landmarks or dense set of points that range in thousands. It is important for the points to be in correspondence which can be done via registration of shapes to each other. For shapes, the distribution of points can be modeled as a multivariate normal distribution in three dimensions[36]

$$s \sim N(\mu, \Sigma) \quad (3.1)$$

$$\mu = \frac{1}{n} \sum_{i=1}^n \vec{x}_i \quad (3.2)$$

$$\Sigma = \frac{1}{n-1} \sum_{i=1}^n (\vec{x}_i - \mu)(\vec{x}_i - \mu)^T \quad (3.3)$$

the training data is used to estimate the mean μ and the covariance matrix Σ . This is estimated using PCA and leads to a model of the form

$$x = \mu + \sum_{i=1}^n \alpha_i \sqrt{d_i} \vec{u}_i \quad (3.4)$$

where d_i and u_i are the eigenvalue/eigenvector pairs.

A Gaussian process is a statistical model used to model data that is defined on a continuous domain such as time or space. It is completely defined by the mean and covariance functions. It can be interpreted as a Gaussian distribution over functions. Functions are infinitely long vectors containing the values of function at every point in the input space. For an input space X , let $f : X \rightarrow \mathbb{R}$, then f is a Gaussian

process if for input vectors $x = [x_1, \dots, x_n]^T, x_i \in X$, the vector containing $f(x) = [f(x_1), \dots, f(x_n)]^T$ is Gaussian distributed.

Luthi et. al[36] apply this idea to shape analysis by modeling variations in shape by modeling the deformations between a set of shapes as a gaussian process. These deformations are added to a reference shape to get a new shape instance. The Karhunen-Loève expansion allows GP to be represented in terms of an orthogonal set of basis functions and gives the form

$$f \sim \mu(x) + \sum_{i=1}^n \alpha_i \sqrt{\lambda_i} \phi_i(x) \quad (3.5)$$

which is similar to PCA. This implies that the eigen values and eigen functions define the variance around a mean shape.

The deformation fields are learned from a set of training surfaces X_1, \dots, X_n . This is done by establishing correspondence between a reference surface and each individual training surface such that a set of deformation fields is obtained where the fields map a point on the reference to the point on the training surface. The Gaussian process is then obtained by estimating the sample mean and covariance function.

Another interesting feature of Gaussian processes is that the covariance function need not be estimated from the sample dataset. Any valid positive definite covariance function can be used. This allows us to define zero mean Gaussian process over a mean shape with an arbitrary smooth covariance function that describes the shape variation. One of the most commonly used function is the Gaussian kernel[36],

$$k_g(x, y) = \exp(- \| x - y \|^2 / \sigma^2) \quad (3.6)$$

$$k(x, y) = s \cdot I_{3 \times 3} k_g(x, y) \quad (3.7)$$

is the matrix form where s is the scale factor that determines the variance of a vector. The covariance function or the kernel function defines the characteristics of the deformation fields. In shape modeling, the deformations are smooth over a region i.e. the points in the same neighborhood are correlated. By applying a smooth kernel, the points in the same neighborhood experience change relatively similarly. This is controlled by the parameter σ or the bandwidth of the kernel. If this value is small, the changes will be correlated between points over a small radius. In other words, small local changes will be modeled. In real world values, the unit for σ is in *mm* and the points in that radius will experience smooth deformations. The scale factor s controls how far a point will move from its mean position i.e. how large the deformation of the point is going to be. These values can be controlled based on the application and will directly influence the flexibility, i.e. its ability to represent new shapes, of a model.

Gaussian process models really shine because they can be easily extended by using multiple kernels. Since the kernels are positive definite kernels, a sum of kernels is also positive definite. This allows for multiple kernels to be added together in order to extend the shape model. A case where this could be done is when there is limited amount of training data. In this case, the model can be extended by adding a smoothing kernel to the sample covariance kernel which is estimated from the example data. Another case where this can be used is to take a multi-resolution approach to modeling local and global shape variations. This gives a flexible approach to developing shape models. By estimating the variation in shape from limited training data, flexible models can be created by extending these variations by

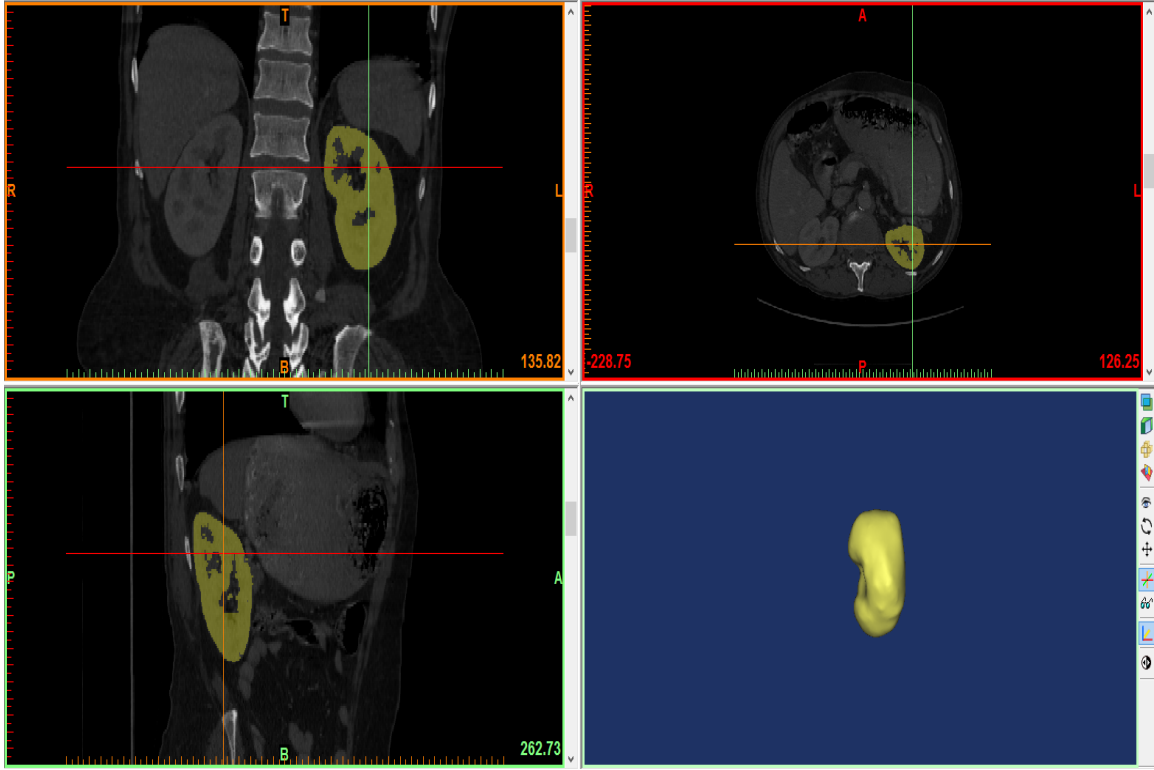


Figure 3.1: Screen capture of the segmentation workflow in Mimics.

adding multiple kernels together.

3.2 Methods

The kidney dataset was acquired from the cancer imaging archive[xx]. The dataset was segmented using Mimics in order to obtain closed triangular meshes of the kidneys.

The meshes were then aligned using rigid coherent point drift algorithm[40]. This algorithm considers the alignment of two point sets as a probability density estimation problem. The surface points can be considered as observations of a probability distribution. In CPD, one of the surface points represent centroids of a Gaussian

mixture model (GMM) and the other point set represents data points. The goal is to fit the centroids to the data points by maximizing the likelihood. The crux is to get the centroids to move as a group in order to preserve the topological structure of the point set. At convergence, the point sets become aligned and the posterior probability of GMM gives the correspondence. The advantage of using this method is that its very robust to noise, outliers, and missing points.

In coherent point drift, the alignment of two D-dimensional point sets, $X_{N \times D} = (x_1, \dots, x_N)^T$ and $Y_{M \times D} = (y_1, \dots, y_M)^T$, is treated as a probability density estimation problem where $Y_{M \times D}$ represents the GMM centroids and $X_{N \times D}$ the data points[40]. The probability density function for the GMM is then written as,

$$p(x) = \sum_{m=1}^{M+1} P(m)p(x|m) \quad (3.8)$$

To take into account noise and outliers the density function takes the following form,

$$p(x) = w(\frac{1}{N}) + (1 - w)\sum_{m=1}^{M+1}(\frac{1}{M})p(x|m) \quad (3.9)$$

where the weight $w(0 \leq w \leq 1)$ takes into account the probability of an observation being classified as an outlier, and $p(x|m) = \frac{1}{(2\pi\sigma^2)^{\frac{3}{2}}} \exp(-\frac{\|x-y_m\|^2}{2\sigma^2})$ [40].

The locations GMM centroids are then adjusted based on some transformation parameters θ . The two unknowns θ and σ^2 are then found by using Expectation Maximization (EM) algorithm. Before the expectation step (E-step) the initial values of transformation parameters (rotation, scale and translation) are initialized to unit values and the variance σ^2 is estimated from the data as,

$$\sigma^2 = \frac{1}{3NM} \sum_{n=1}^{N+1} \sum_{m=1}^{M+1} \|x_n - y_m\|^2 \quad (3.10)$$

In the E-step the posterior probability, which defines the correspondence between two points x_n and y_m , is estimated as,

$$P(m|x_n) = \frac{\exp^{-\frac{1}{2} \left\| \frac{x_n - T(y_m, \theta)}{\sigma} \right\|^2}}{\sum_{k=1}^M \exp^{-\frac{1}{2} \left\| \frac{x_n - T(y_k, \theta)}{\sigma} \right\|^2} + (2\pi\sigma^2)^{3/2} \frac{w}{1-w} \frac{M}{N}} \quad (3.11)$$

where $T(y_m, \theta)$ is the transformation applied to Y [40].

In the maximization step (M-step) the new values for transformation parameters and σ^2 are estimated by minimizing the following objective function,

$$Q(\theta, \sigma^2) = \frac{1}{2\sigma^2} \sum_{n=1}^{N+1} \sum_{m=1}^{M+1} P^{old}(m|x_n) \|x_n - T(y_m, \theta^{old})\|^2 + \frac{3N_P}{2} \log \sigma^2 \quad (3.12)$$

where $N_P = \sum_{n=1}^{N+1} \sum_{m=1}^{M+1} P^{old}(m|x_n)$. The *old* superscript denotes that the values used for calculating are from the previous iteration.

The EM steps iterate until the variance σ^2 falls below a threshold value. The new variance calculated at each iteration is,

$$\sigma^2 = \frac{1}{3N_P} \sum_{n=1}^{N+1} \sum_{m=1}^{M+1} \|x_n - T(y_k, \theta)\|^2 \quad (3.13)$$

The transformation $T(y_k, \theta)$ is different based on the type of registration in use (rigid, non-rigid or affine) and an in-depth discussion of the details can be found in Myronenko and Song[40][41].

Once the datasets are aligned using CPD, a reference shape of the kidney needs to be generated. The reference shape is generated to minimize the bias of the shape model towards one particular instance from the training data. For performing the registration to get point correspondences as well as to generate the shape model, we use the tools provided with the open-source toolkit Statismo[35].

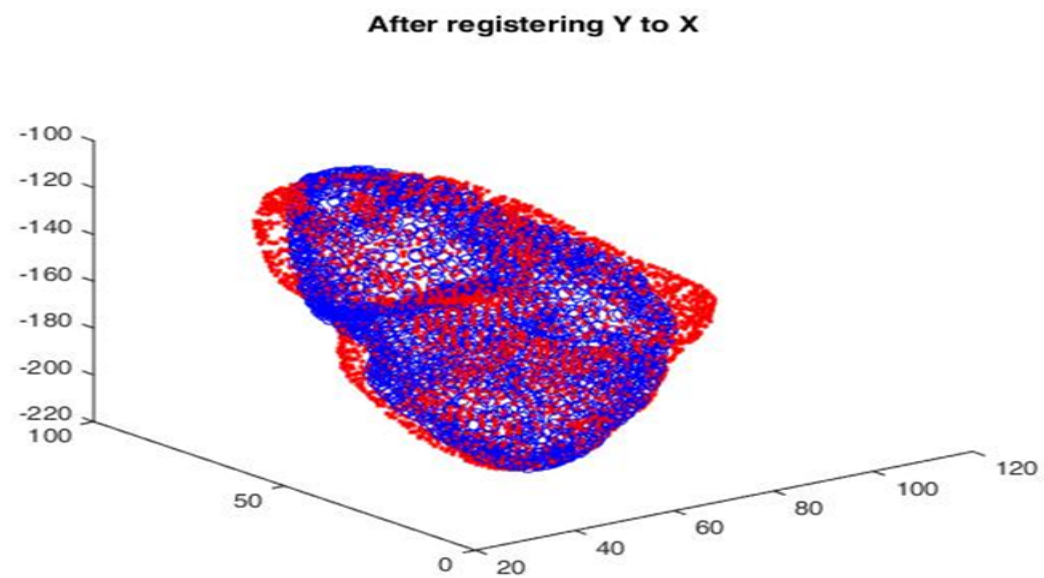
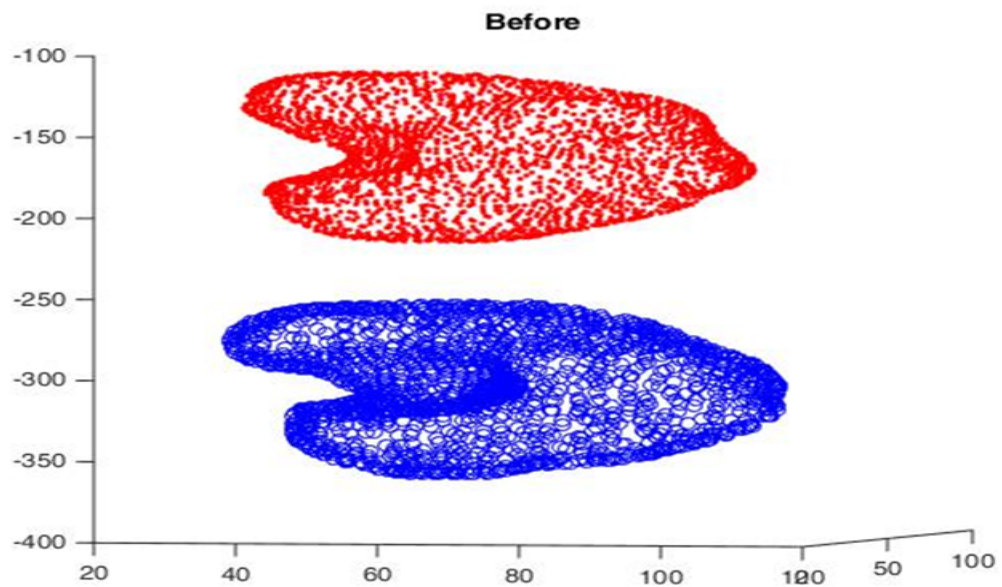


Figure 3.2: Kidney datasets before and after rigid CPD alignment.

In order to generate a reference shape, a zero mean Gaussian process is built on an arbitrarily chosen shape from the training sample using a Gaussian kernel. The bandwidth σ used was 50 *mm*. Larger value of the bandwidth will model larger deformations i.e. on a more global scale whereas, smaller value will focus on smaller variations at a more local scale.

Before building the shape model, in order to learn the deformations from the training data, all the training samples need to be in correspondence with each other. In order to do so, a second registration step is required. Luthi et. al[37] present a novel approach to use a Gaussian process model to establish correspondence (Registration) via shape fitting. In this approach, registration is viewed as an optimization problem to find a deformation field that maps points on the reference surface to the target surface. The optimization problem is of the form,

$$\hat{u} = \arg \min_{u \in F} D[\Gamma_R, I_T, u] + \eta R[u] \quad (3.14)$$

where D is a distance metric between the target and reference surface, R is a regularizer term[37] and u is the component that parametrizes the transformation, in this case it is a shape model.

For a Gaussian process, as described previously, the deformation can be expressed as,

$$u(x) = \mu(x) + \sum_{i=1}^n \alpha_i \sqrt{\lambda_i} \phi_i(x) \quad (3.15)$$

The equation 3.7 takes the form,

$$\hat{u} = \arg \min_{\alpha_1, \dots, \alpha_n} \sum_{x_j \in \Gamma_R} D_T(x_j + \mu(x_j) + \sum_{i=1}^n \alpha_i \sqrt{\lambda_i} \phi_i(x_j))^2 + \eta \sum_{i=1}^n \frac{\alpha_i^2}{\lambda_i} \quad (3.16)$$

Here D_T is the distance map of the target surface. The shape model is fitted

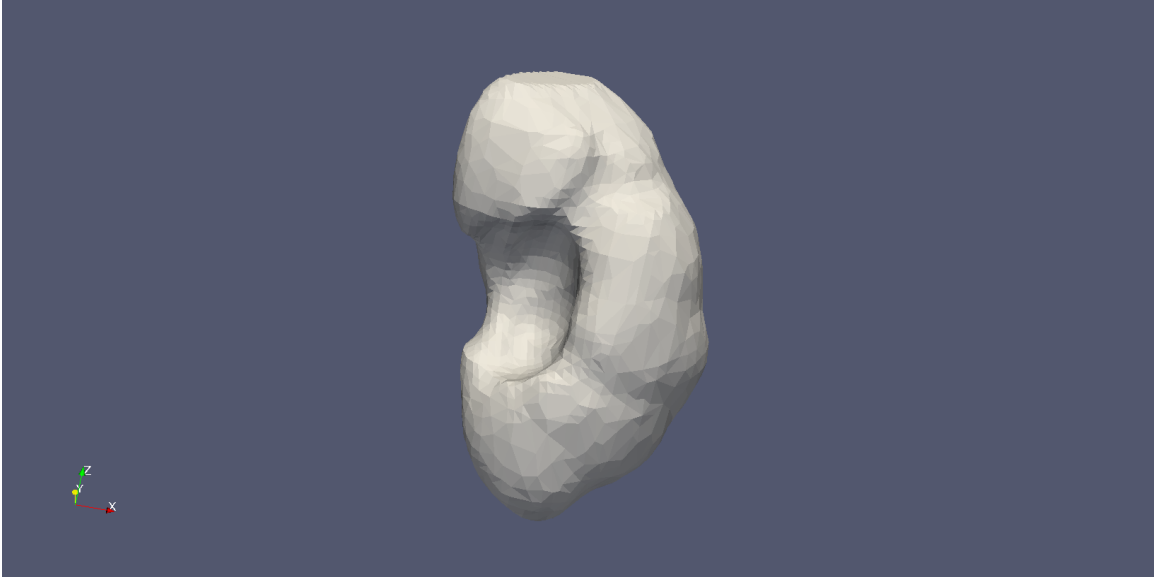


Figure 3.3: Reference kidney shape generated iteratively.

to the distance map of the target surface as this is computationally efficient as implemented in ITK. The implementation of this algorithm that is provided with Statismo utilizes Euclidean distance map for the target image. They also use a LBFGS optimizer with a mean squared metric. More details can be found in [35] and [37]. The goal of this step is to deformably fit the shape model to the target surface so as to get an instance of deformed reference shape that is in one to one correspondence with the target surface.

The Gaussian process model built previously on an arbitrary training shape is fit to all the shapes in the training set. Once they are in correspondence, a mean shape is calculated. The Gaussian process model is rebuilt on this mean shape and the same process of registering with rest of the training sets is repeated. The mean shape from every step is compared to the previous step via the average distance between the meshes. This process is repeated till the mean shapes show very little change. This is then chosen as the final reference shape.

The training set is then brought into correspondence with the reference shape and is subjected to principal component analysis. The model is of the form,

$$\textit{new shape} = \textit{mean} + \textit{linear combination of eigen values and eigen vectors}$$

As the amount of training data will always be a limiting factor, there will always be a bias. Taking advantage of Gaussian process, the PCA model can be extended to be more expressive by adding a Gaussian kernel to the kernel learned from the training data as discussed previously. In this case in order to build an extended model a Gaussian kernel was added with a bandwidth value of σ 100 *mm* and scale value s of 10 *mm*.

The shape model is then evaluated over three metrics. Compactness, Generalization and Specificity. Compactness of a model is its ability to describe a shape instance with as few principal components or modes as possible. It is calculated as the cumulative variance of the model as a function of number of modes. A compact model should be able to capture most of the variance in the shape with as few modes M as possible. It is calculated as,

$$C(M) = \sum_{i=1}^M \lambda_i \tag{3.17}$$

The generalization is the ability of a model to represent an unseen instance of an object. It is a property that can describe how well the model is able to capture the possible variation in shape from its training data. In order to measure generalization, a model is first built from a set of training data. The model is then fit to an unseen test sample. The quality of fit is measured as the average distance between the target shape and the shape instance from the model that best describes the unseen shape. This is done for a set of test samples and the average distance (error metric in this case) is calculated for the entire test set. Generalization is again measured as a

function of modes used to describe the shape model.

$$G(M) = \frac{1}{n_{tr}} \sum_{i=1}^n D_i(M) \quad (3.18)$$

where n_{tr} is the number of samples in the training set and D_i is the average distance between two shapes.

Specificity of a model describes the ability of a model to generate instances of the shape that are similar to those in the training set. This means that the model is able to generate instances that are anatomically accurate representations. For measuring how specific the model is, a set of instances is sampled from the model and are compared to the shapes in the training set. It is measured as the average distance between the sampled shapes and their closest representation in the training set.

$$S(M) = \frac{1}{N_s} \sum_{i=1}^N D_i(M) \quad (3.19)$$

where N_s is the number of sample instances generated from the shape model and D_i is the average distance between two shapes.

3.3 Results

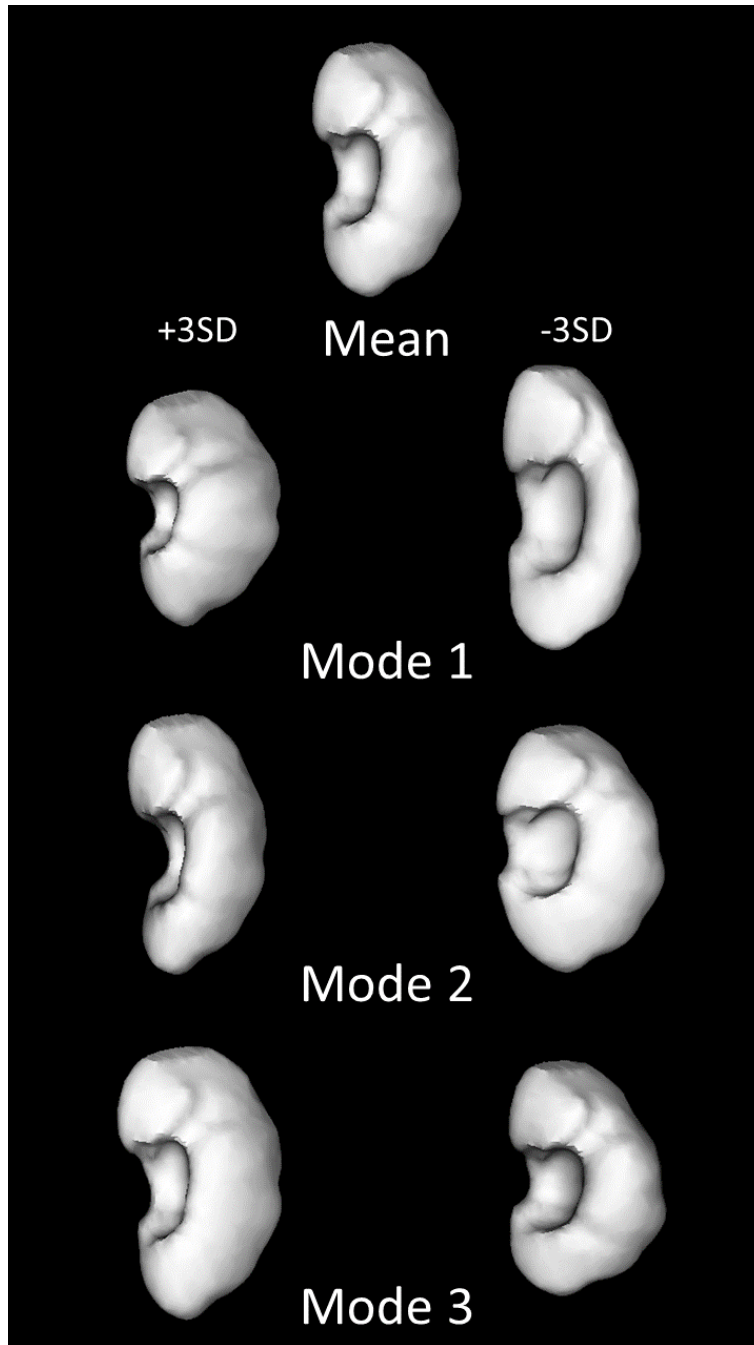


Figure 3.4: Samples from PCA shape model with samples from first three modes representing $\pm 3SD$.

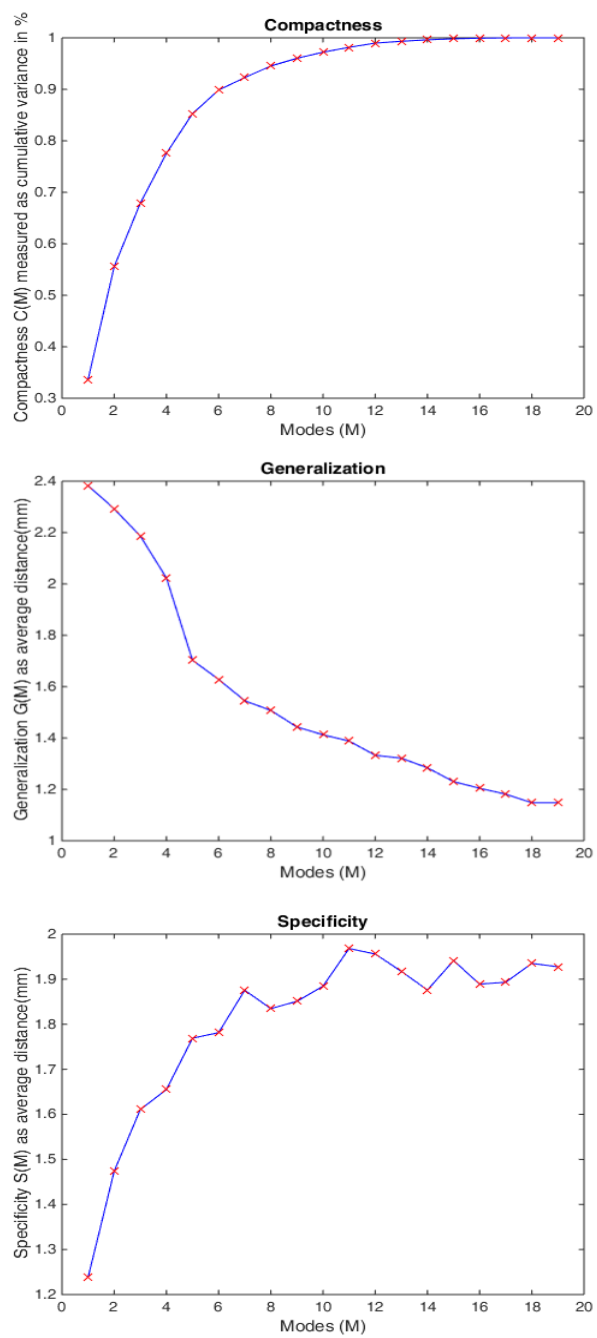


Figure 3.5: Metrics for assessment of the shape model.

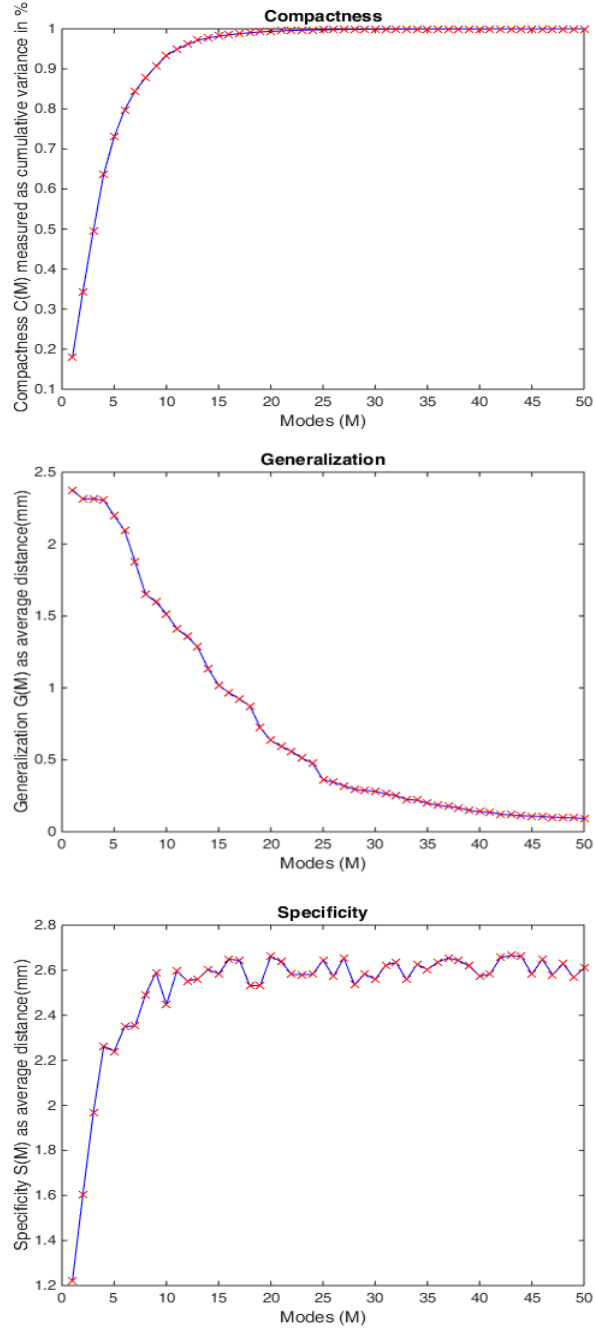


Figure 3.6: Metrics for assessment of the extended shape model.

The Figure 3.3 shows the variation in shape learned from the kidney training set. The first mode of the model typically shows the most variation in the shape

as compared to the subsequent modes. It is also important to note that the model represents anatomically realistic shapes.

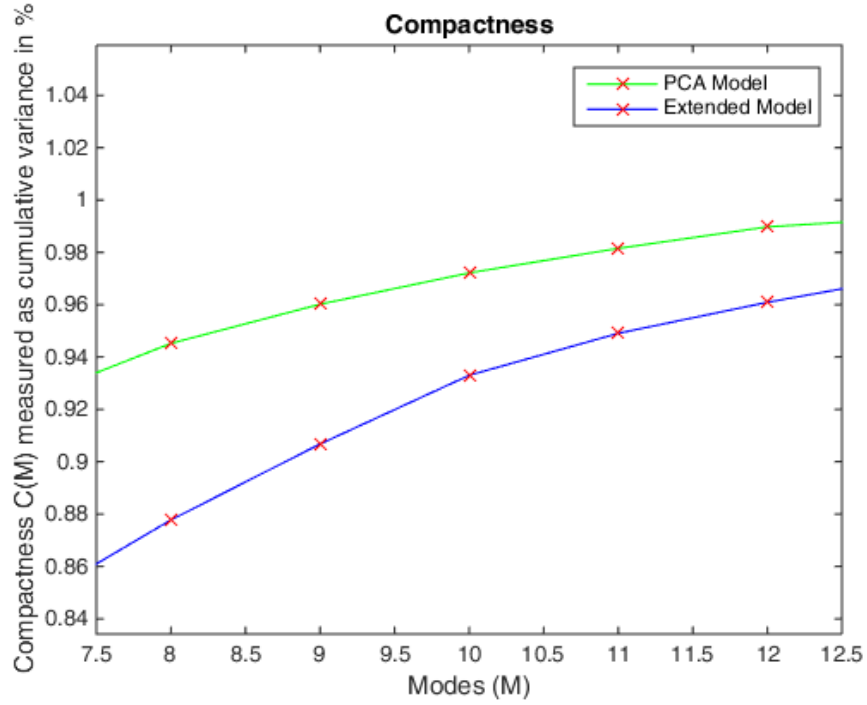


Figure 3.7: Comparison of compactness between PCA model and Extended model.

The assessment of the PCA model and the extended model show that they are able to capture around 96% and 93% of the total variance in the data in the first 10 modes respectively. This indicates that both the models are sufficiently compact, i.e. they represent majority of the variation in relatively small number of modes. What this implies is that the model can be expressive enough with reduced dimensionality from the original data.

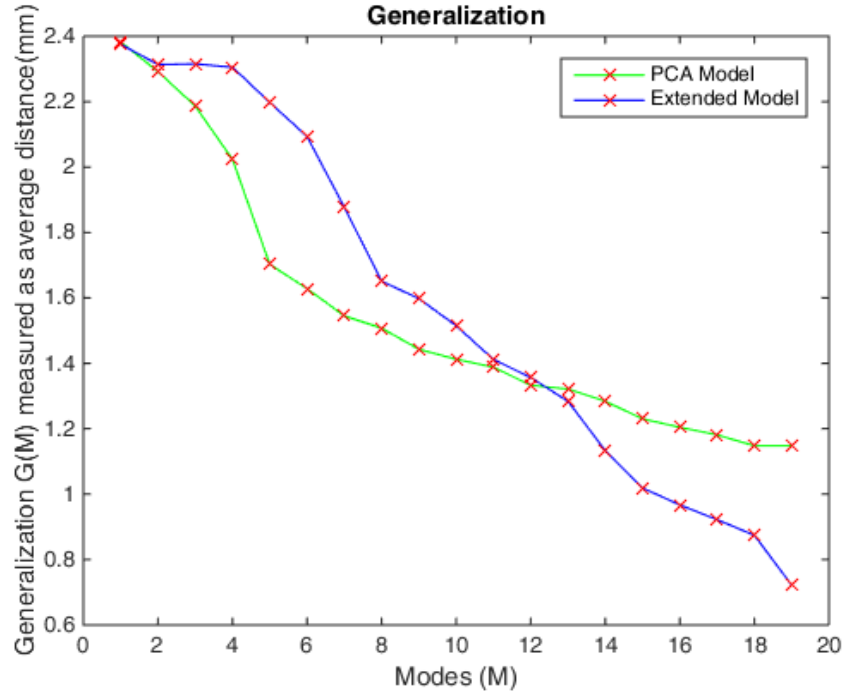


Figure 3.8: Comparison of generalization between PCA model and Extended model.

The generalization metric indicates how well the model can represent new shapes that the model has not seen previously. Figure 3.3 shows that for the PCA model the error ranges from 2.4 mm for one mode to a reduced error of around 1.2 mm for 19 modes. For the extended model the error further reduces below 1 mm after 15 modes. This implies that both the models are able to accurately represent shapes from the test sample with the performance of the extended model improving with increasing modes. This can be attributed to the fact that the PCA model was extended using a Gaussian kernel to model smooth deformations. This increased the variance in shape, in terms of real world dimensional distances, for every principal mode in addition to what was learned from the sample data. This enables the extended model to better represent some shapes in the test set, thereby reducing the average distance metric.

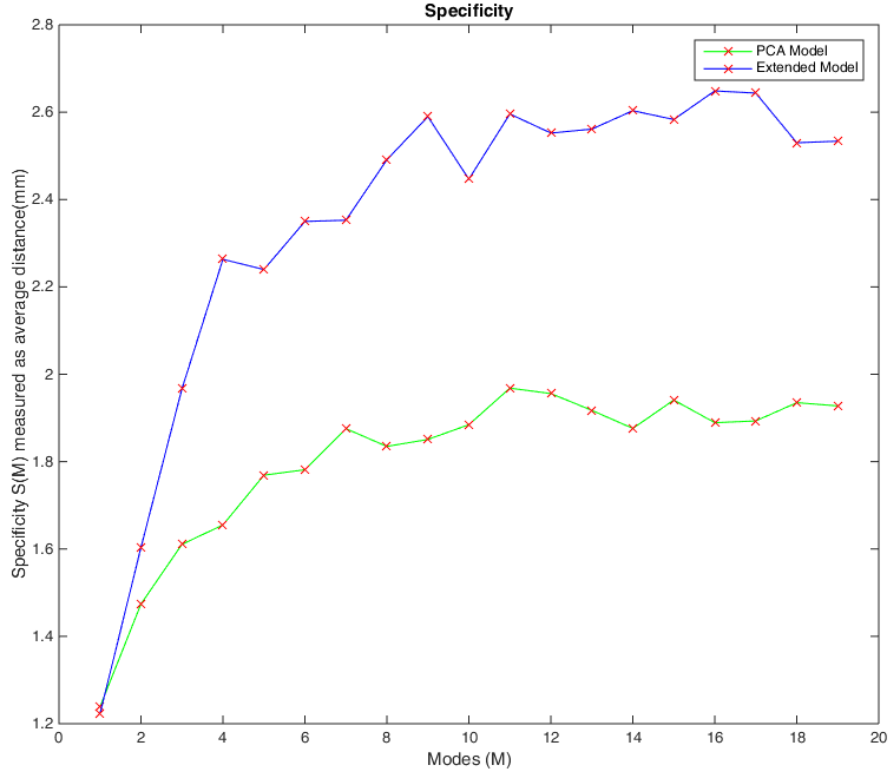


Figure 3.9: Comparison of specificity between PCA model and Extended model.

The specificity of the PCA shape model is slightly better than the extended model. This can be attributed to the fact that extending the model might have produced samples that were very different from the training dataset. As a result there is a higher average error. But as it can be seen from the above graph, the difference between the two is less than 1 mm and hence both the models represent good specificity in terms of expressing the shape that the model is defined to describe.

3.4 Summary

Statistical shape modeling utilizes statistical analysis to analyze geometrical properties of shapes and to model the variation seen in a population. In this work we build a shape model of the kidney on a set of shapes segmented from CT image dataset. The differences in shape within a population can be parametrically defined by a shape model. In order to do so, we first align a set of segmented shapes in a common frame of reference using the rigid coherent point drift algorithm. Correspondence matching was then done on these aligned shapes using a modified version of the iterative closest point algorithm. The shapes once in correspondence are then subjected to principal component analysis. PCA reduces the dimensionality of data and allows for the representation of shapes with a few orthogonal basis functions. The new shape instance can be represented as a sum of the mean and a linear combination of the eigenvalues and eigenvectors of the covariance matrix, which describes the variation of the shape from the mean. In the presence of limited training data, the shape model can be over constrained and can introduce bias towards generating instances of shapes that will closely match the training data.

In order to improve up on this, we utilize the concept of Gaussian processes to expand the flexibility of the model. The Karhunen-Loève expansion of a Gaussian process makes it similar to the representation of PCA model. We utilize this to expand the covariance kernel learned from the data by defining a zero-mean Gaussian process over the PCA model and adding a smooth covariance kernel based on a Gaussian function. The scale and the bandwidth of the function control the variation of individual points and hence the shape. The bandwidth of the kernel controls how many points in a neighborhood are correlated. This controls the smoothness of the deformations. Larger values of the bandwidth parameter will allow for more global de-

formations as mode points are correlated where as a smaller value will model smaller, local changes. The scale factor controls the amplitude of the variation i.e. how much distance will the points move from their original (mean) location. The value of scale and bandwidth were chosen arbitrarily based on our application. The model is then assessed for compactness, generalization and specificity metrics. Compactness defines how few modes express the maximum amount of variance in shape in the model. For the PCA model 95% variance was captured by 10 modes and for the extended model this was at 13 modes. This indicated that the models were sufficiently compact and could be expressive enough by reducing the number of eigenvectors required to define a shape. The generalization metric is used to assess how well a model represents shape instances it has not seen in the training dataset. This is measured by fitting the shape model to a number of test shapes that were excluded from the training data and the average surface distance is calculated. The extended model performs slightly better as it has more flexibility in terms of representing variability in shape. The specificity metric looks at the ability of the model to represent instances that belong to the shape class. The extended model showed specificity slightly worse than the PCA model.

Chapter 4

Statistical shape modeling based renal volume measurement using tracked ultrasound

4.1 Introduction

Renal volume measurement is of great diagnostic and prognostic value when treating various kidney diseases. Autosomal dominant polycystic kidney disease (ADPKD) is the fourth most common cause of kidney transplant worldwide accounting for 7-10% of all cases. In the United States, one in every twenty cases of end-stage renal disease (ESRD) is caused due to ADPKD[50]. It is a progressive disorder that begins with a relatively small number of cystic renal tubules which expand over time. These are benign fluid-filled tumors that directly invade and displace adjacent parenchyma. Although ADPKD usually progresses over many decades, accurate risk prediction is an important task[50]. This is because identifying patients with progressive disease is vital to providing new treatments being developed and enable them to

enter clinical trials for new therapy. Genotype, age, gender, glomerular filtration rate (GFR) and total kidney volume (TKV) are the major factors predicting the progression of ADPKD. Longitudinal studies conducted by the Consortium for Radiologic Imaging Studies in Polycystic Kidney Disease (CRISP)[1] has shown that TKV is an early and accurate measure of cystic burden and likely growth rate. Increased renal volume predicts and is associated with loss of renal function[15].

Currently, the use of MR is considered as a gold standard measure to monitor TKV accurately. While clinical ultrasound (US) has proven as an excellent tool for diagnosing the disease and assessing long-term changes; monitoring short-term changes using ultrasound has been shown to not be accurate. This inaccuracy can be attributed to high operator variability and inability to accurately reproduce quantitative measures as compared to tomographic modalities such as CT and MR. A study conducted to compare the efficacy of US versus MR for volume measurement showed that using current standard protocols, US show a substantial systemic underestimation to the tune of 25% of renal volume when compared to MR measuring techniques[5], it has been shown that the repeatability of this method is not very good. For inter-observer variation in US renal volumetry, it was observed that the standard deviation spread anywhere from 16% - 48% of the TKV as compared to MR techniques where the variation was in a range of 2% - 3%. However, the correlation between US and MRI volume was shown to be 0.88 - 0.89[44]. This is a very good indicator that US needs to be further explored as a viable modality for precise and reproducible measurement of TKV in ADPKD patients. However, US has shown reasonable correlation with MR in a head-to-head comparison.

Over the past decade, as imaging hardware has advanced, ultrasound has emerged as one of the standout modality for intra-procedural imaging. In parallel to this, the development of hardware and methods for spatial localization has afforded

us the ability to track 2D ultrasound, in three-dimensional, physical space which they are being used. The availability of excellent diagnostic and intra-procedural imaging, combined with the ability to track tools during a procedure, has created new possibilities for the use of imaging for surgery and intervention. In addition to this, the vast amount of recorded tomographic data can be used to generate statistical shape models that allow us to extract clinical value from archived image sets. In this work, we aim at improving the prognostic value of US in managing ADPKD by assessing the accuracy of using statistical shape model augmented US data, to predict TKV, with the end goal of monitoring short-term changes.

4.2 Methods

Step 1: A shape model was developed using the techniques as explained in chapter 3. It was assessed for quality and concluded that the model we have developed for our application is sufficient to represent anatomically correct shapes of kidney.

Step 2: Tissue mimicking phantoms of the kidney were constructed using platinum cured silicone rubber Smooth-on Ecoflex 0030(Smooth-On Inc, Macungie, PA). In order to do this at first positive models of kidneys were hand crafted in order to construct moulds from plaster of paris. Upon curing, silicone rubber was poured in the moulds and phantoms were cast in order to best represent the kidney shapes of various sizes. The kidneys were made to have slightly irregular surface rather than a smooth surface so as to simulate deformity. The cured kidney models were then embedded in gelatin hydrogel crosslinked with Chromium(III) potassium sulphate dodecahydrate. The hydrogel has echoic properties that mimic those seen within tissue when under ultrasound.



Figure 4.1: Kidney phantoms made from Smooth-on Ecoflex0030.

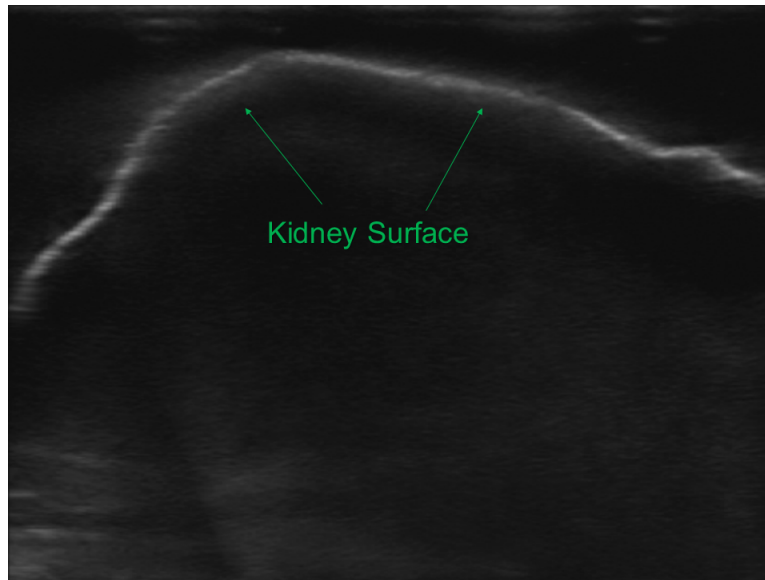


Figure 4.2: Kidney phantom under ultrasound showing partial surface.

Step 3: A tracked ultrasound system as implemented in chapter 2 was used

to scan the phantoms. 3D volume was constructed from these scans for the purpose of manual segmentation.

Step 4: The reconstructed volume was then imported into the open-source 3D Slicer[21] application for the process of segmentation. The kidney was manually segmented in all three axes. During segmentation, when the shape of the kidney was not fully visible, estimation was used to demarcate the boundaries. The goal was to approximately capture the shape of the organ as best as possible from the partial data available from the stack of tracked ultrasound slices. The segmentation mask was then exported as a mesh for further processing. The segmentation mask meshes are partial in nature and need to be converted to a closed mesh. In order to do so a spherical mesh was deformably fit to the segmentation mask. This was done by applying deformable registration to the spherical mask via the non-rigid coherent point drift algorithm. The deformed mesh gives a closed mesh representation of the segmented kidney from the ultrasound data.

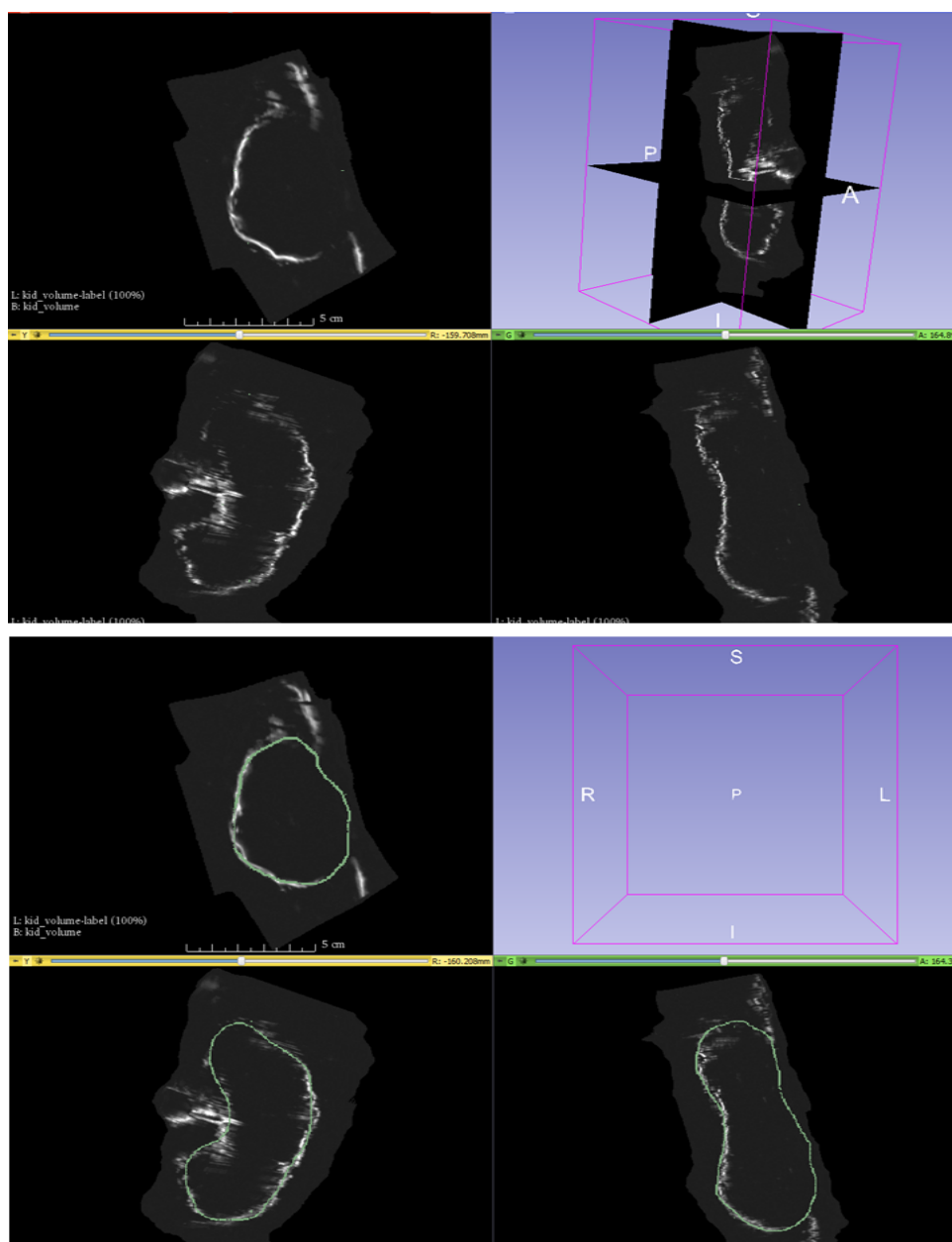


Figure 4.3: Kidney segmentation in 3D slicer. Bottom image shows manual segmentation masks.

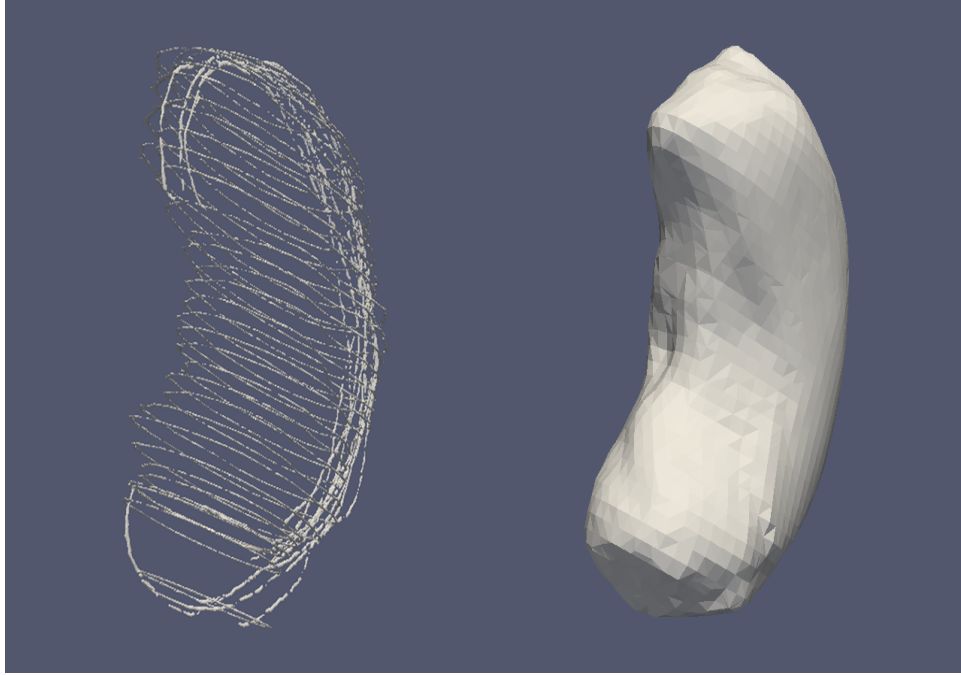


Figure 4.4: Segmentation mask and the deformed sphere fit to the mask to generate a closed mesh representation.

Step 5: The deformed spherical mesh is aligned with the reference shape from the shape model developed in the previous chapter. The shape model was then fit to the deformed mesh to obtain the best instance that describes the shape of the deformed spherical mesh. Calculating the volume of an enclosed mesh is relatively a simple solution due to an elegant method presented in Zhang et. al[65]. The idea is to calculate the volume of each tetrahedron that makes the surface mesh assuming it has the origin at $(0, 0, 0)$.

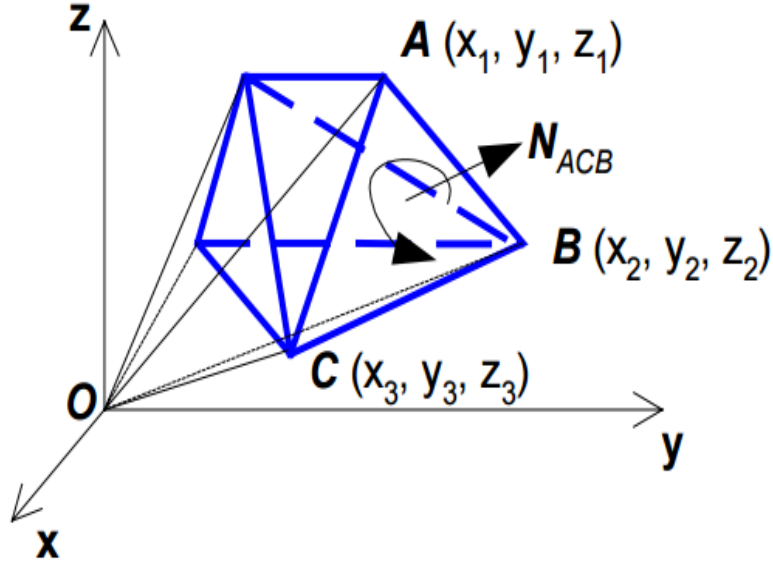


Figure 4.5: Illustration of a unit tetrahedron used for calculating the volume of a triangular mesh.

The volume for individual tetrahedron is then calculated as,

$$|V_{OACB}| = \left| \frac{1}{6}(-x_3y_2z_1 + x_2y_3z_1 + x_3y_1z_2 - x_1y_3z_2 - x_2y_1z_3 + x_1y_2z_3) \right| \quad (4.1)$$

where A, B, C are the vertices of a surface triangle. This gives us a signed-volume of the triangle (tetrahedron). To get the total volume we add up the signed volumes of each triangle.

$$|V_{total}| = |\Sigma_i V_i| \quad (4.2)$$

where i stands for the index of individual surface triangles.

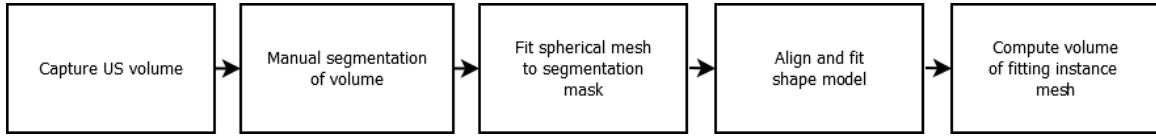


Figure 4.6: Workflow for volume calculation.

The true volume of the kidney phantoms is determined by volume displacement test. The phantoms are individually placed in a water bath in a measuring beaker. The volume is calculated by measuring the difference in water displaced once the phantom is completely immersed in the water. This gives the gold standard volume for the phantoms against which our method will be examined.

In order to test the feasibility of our method, two experiments are designed. The first one involves asking participants to scan the kidney phantoms using a tracked ultrasound. The goal of this is to see how well the participants could acquire kidney shape. The ultrasound probe in use is a linear array with frequency range of 6-15MHz. As seen in a typical clinical scenario, capturing large sized kidneys is not trivial as the entire organ can not be imaged in a single plane. But taking advantage of using a tracked US system, the entire extent of the kidney can be captured by stacking multiple pose tracked 2D frames. These frames are then converted to a 3D volume and the organ boundaries are demarcated by individual with segmentation experience.

In the second experiment, the participants are given a set of kidney volumes and are asked to segment the organ boundaries. The participants are given a brief training on how to segment the region of interest. The goal in this scenarios is to see how well the method works in order to calculate the kidney volume when segmented by multiple subjects.

4.3 Results

Table 4.1: Volume calculated from segmentations done by subjects and the corresponding absolute percentage difference in volume from gold standard volume of 175 mL for Phantom 1

Subject	Volume (mL)	Absolute Percentage Difference
1	177.09	1.19
2	178.99	1.28
3	176.06	0.60
4	193.79	10.74
5	193.12	10.35
6	186.02	6.30
7	175.98	0.56
8	172.86	1.22
9	152.55	12.83
10	168.16	3.91

Mean \pm SD	177.46 \pm 12.11	4.99 \pm 4.72
---------------	--------------------	-----------------

Table 4.2: Volume calculated from segmentations done by subjects and the corresponding absolute percentage difference in volume from gold standard volume of 266 mL for Phantom 2

Subject	Volume (mL)	Absolute Percentage Difference
1	245.74	7.62
2	249.66	6.14
3	254.41	4.35
4	253.45	4.72
5	268.33	0.87
6	266.96	0.36
7	234.66	11.78
8	266.75	0.28
9	235.85	11.33
10	246.76	7.23
Mean \pm SD	252.26 \pm 12.24	5.47 \pm 4.19

Table 4.3: Volume calculated from segmentations done by subjects and the corresponding absolute percentage difference in volume from gold standard volume of 200 mL for Phantom 3

Subject	Volume (mL)	Absolute Percentage Difference
1	181.71	9.15
2	206.82	3.41
3	209.75	4.88
4	181.50	9.25
5	214.22	7.11
6	203.75	1.88
7	198.73	0.64
8	202.35	1.18
9	172.02	13.99
10	184.60	7.70
Mean \pm SD	195.55 \pm 14.89	5.91 \pm 4.28

Renal volumetry is of great interest in the management of chronic kidney diseases (CKD). In polycystic kidney disease, kidney volume has a strong prognostic indication of declining function. While ultrasound has played an important role in diagnosis, its use as a modality with high prognostic value is limited. In our work, we take advantage of tracked ultrasound to generate a stack of images and in turn a volume of our region of interest. In this case, our volume of interest should capture the extent of kidney phantoms. Fitting a statistical model to the acquired volume

mesh, we are able to generate a possible instance that best represents the anatomical shape of the scanned phantom.

Table 4.1, 4.2, 4.3 show the volumes calculated by our method when phantoms 1, 2 and 3 were segmented by 10 different subjects. The absolute percentage difference between the calculated volume and the gold standard volume of the phantom is derived. One sample t-test was performed and it was noted that the percentage error in wrongly estimating the volume when compared to the gold standard was less than 10% ($p < 0.05$) for all three phantoms.

We also looked at the ability of our method to discern the volume change between individual phantoms. This is important as it can indicate if the method is able to detect a relatively small change in volume. Again the absolute percentage difference between two phantom volumes was calculated and compared to the actual difference in their gold standard volumes. It was seen that between phantom 1 and 2, where the difference was 91 mL, our method could discern the volume with an estimation error of up to 25% ($p < 0.05$). Between phantom 2 and 3, where the difference was 66 mL, the error of estimation was up to 27% ($p < 0.05$). For a small change of 25 mL between phantom 1 and 3, the error was too large and volumes could not be told apart reliably.

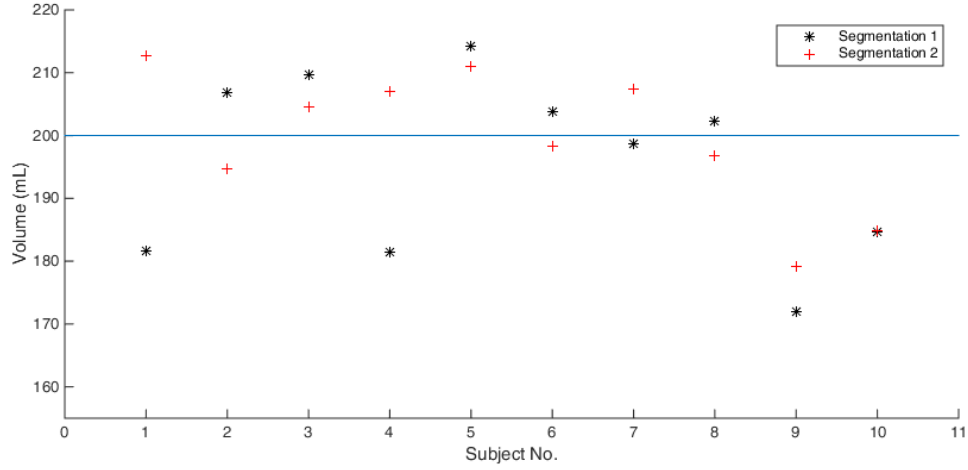


Figure 4.7: Scatter plot showing the volumes obtained by segmenting the same phantom twice by subjects.

The participants were also made to segment phantom 3 images twice, once as the first set for segmentation and second after having segmented the other two phantoms. It can be observed from the scatter plot (Figure 4.7) that majority of the participants demonstrated good repeatability in their segmentations that led to good agreement in volume reading between the two measurements. There were two outliers where the volume calculations showed a difference of around 25.16 and 31.04 mL.

In addition, the scans obtained from the participants scanning the phantoms were segmented by individual with prior segmentation experience. It was again observed that the absolute percentage difference between the actual volume and the calculated volume of the phantom was wrongly estimated by an error of upto 10% ($p < 0.05$) for all three phantoms. This indicates that the volume can be reliably calculated by someone with prior segmentation experience as well as someone without prior segmentation experience within a reasonable amount of over or under estimation.

It is important to note that manual segmentation is prone to wrong demarcation of organ boundaries. Even though the segmentation relies on the user's knowledge of anatomical shape, in the cases where the entire extent of the organ is not known the method is prone to underestimating the volume. This could be a realistic scenario when scanning kidneys of very large size.

In conclusion, we have presented a new method to measure the volume of a kidney using tracked ultrasound augmented by statistical shape model. Once the approximate segmentation of the organ is obtained from reconstructed volume, applying shape model to the segmentation produces an instance that is anatomically accurate based on the shape model that is trained using ground truth segmentations from CT scans.

Chapter 5

Conclusion and Future Work

In this work we present a novel approach to measuring renal volume using tracked ultrasound and statistical shape models. In our work, the goal was to utilize tracked 2D ultrasound to recover 3D shape information for the kidney in order to calculate the volume of the organ. The polaris tracking system was used to track the ultrasound probe in 3D space and using the tools provided in the PLUS toolkit, this information was used to map the pixel coordinates from the image plane to real world 3D coordinates. In order to do this two step calibration was performed. The entire system is loosely coupled of components which comprises of tracking system, ultrasound interfaced to a PC via a frame grabber and the processing software on the PC, at first a temporal calibration scheme was performed. This ensured that all the data streams were in sync and the pose information acquired from the tracking system accurately corresponded with the image information gathered from the ultrasound system via the frame grabber. Following this, a spatial calibration was performed using a N-wire phantom. Spatial calibration is a vital step as it is important to obtain the position of a feature of interest in the image plane in terms of its real world coordinates. In the system implemented here, we used a linear array with

frequency from 6-15 MHz that was calibrated for an imaging depth of 6 cms.

We then developed a statistical shape model of the kidney using 20 segmented kidney CT scans. The differences in shape within a population can be parametrically defined by a shape model. In order to do so, we first align a set of segmented shapes in a common frame of reference using the rigid coherent point drift algorithm. Correspondence matching was then done on these aligned shapes using a modified version of the iterative closes point algorithm. The shapes once in correspondence are then subjected to principal component analysis. PCA reduces the dimensionality of data and allows for the representation of shapes with a few orthogonal basis functions. The new shape instance can be represented as a sum of the mean and a linear combination of the eigen values and eigen vectors of the covariance matrix, which describes the variation of the shape from the mean. In the presence of limited training data, the shape model can be over constrained and can introduce bias towards generating instances of shapes that will closely match the training data.

In order to improve up on this, we utilize the concept of Gaussian processes to expand the flexibility of the model. The Karhunen-Loève expansion of a Gaussian process makes it similar to the representation of PCA model. We utilize this to expand the covariance kernel learned from the data by defining a zero-mean Gaussian process over the PCA model and adding a smooth covariance kernel based on a Gaussian function. The scale and the bandwidth of the function control the variation of individual points and hence the shape. The bandwidth of the kernel controls how many points in a neighborhood are correlated. This controls the smoothness of the deformations. Larger values of the bandwidth parameter will allow for more global deformations as more points are correlated where as a smaller value will model smaller, local changes. The scale factor controls the amplitude of the variation i.e. how much distance will the points move from their original (mean) location. The

value of scale and bandwidth were chosen arbitrarily based on our application. The model is then assessed for compactness, generalization and specificity metrics.

We then created a work flow to extract shape data from kidney phantoms using tracked ultrasound and to compute the volume of the scanned phantoms. For this we manufactured kidney shaped phantoms from platinum cured silicone rubber and embedded them in gelatin hydro-gel. The phantoms were then scanned using the tracked ultrasound system and volume was reconstructed. On these reconstructed volumes, participants were asked to segment the kidney shape in the axial plane. In every image, there was a part of the phantom that was occluded due to limited angles for scanning. These parts were approximated based on anatomical knowledge to complete the segmentation masks. A spherical mesh was then deformed and fit to the segmentation masks and eventually the shape model was fit to obtain an closest anatomical instance to the scanned kidney. The volume was then calculated on this instance. It was observed that the volume was approximated correctly with up to a 10% error from the gold standard volume of each phantom, which was measured by the water displacement method. In addition we also saw that the method could differentiate between volumes with an error of up to 25% for 91 mL difference and an error of upto 27% for a difference of 66 mL between phantoms. This is a positive indication that small changes in volume can be identified, but the results need to be treated with caution as more tests are required.

Future work can investigate the construction of statistical shape model of a polycystic kidney. Polycystic kidneys are large and highly irregular in shape. The heterogeneity of the organ shape is challenging aspect that needs to be modeled. This can potentially be done using a multi-scale kernel approach using Gaussian processes. Deformations on multiple scales can be modeled using a linear combination of kernels. This combination includes kernels with larger bandwidth which model

global, smoother deformations where as kernels with decreasing scales and bandwidths focus on more local changes that capture details.

Another aspect that needs to be investigated is to build active appearance models in addition to shape knowledge to help in semi-automatic segmentation of the organ. This can be done by manufacturing more realistic phantoms that mimic echogenicity of the kidney. Materials such as poly vinyl alcohol cryogel (PVA-C) have shown to have excellent echogenicity and could be used to manufacture phantoms that will allow for the extraction of appearance related information. In addition, models can be developed on kidney data directly taken from the patients.

Appendices

Appendix A Using curvelet transform for edge detection and segmentation of tissue

A.1 Introduction

Supraspinatus, along with the Infraspinatus, the Subscapularis, and the Teres-minor form the major muscles of the rotator cuff. Of these, supraspinatus tendon disorders rank as the third most commonly occurring musculoskeletal pathology, primarily caused by inflammation, partial, or full thickness tears. It results in severe discomfort and reduced mobility of the shoulder accompanied by acute or chronic pain. The chronic tear of the rotator cuff can develop slowly over an extended period of time and is usually not detected at the initial stages because symptoms (such as pain, weakness accompanied by stiffness, and loss of motion) worsen slowly over time. This makes detection, management, and staging of the disease critically important. This is especially true in high-risk groups such as athletes that are involved in activities warranting overuse of the shoulder. Towards this end, in our previous work, we have developed novel real-time techniques to biomechanically assess the condition of the rotator cuff in order to manage the disease and to guide therapy[46, 32, 58]. Our technology is based on the Musculoskeletal Ultrasound (MSK-US), which is seeing widespread use in the assessment of soft tissue orthopedic disorders. Ultrasound has been shown to have a higher degree of sensitivity in diagnosing tears when compared with the gold standard MRI. In order to do ex-vivo assessment using our techniques, there is a need for good segmentation and classification approaches to identify the tissue in question. However, segmentation of a region of interest automatically from ultrasound remains a long studied and challenging area of research due to poor contrast, intrinsic noise, and operator variability.

In this work, we propose a novel approach to the possibility of using curvelet transforms for automatic edge and feature extraction. Curvelets have shown to present an optimal multi-scale representation of edges in images. They are designed to efficiently represent edges and singularities along the curves in images[10]. The curvelet coefficient values depend on how well they align with an edge and, subsequently, the curve. The best alignment is represented by the highest coefficient value, with the values of unaligned curvelets tending to zero (Figure 1). This gives us the ability to identify edges as well as the direction of the curve efficiently. This property of curvelet transform makes it a very attractive proposition for use in selectively extracting edges in US images, specifically for a tissue such as supraspinatus which has a highly directional appearance.

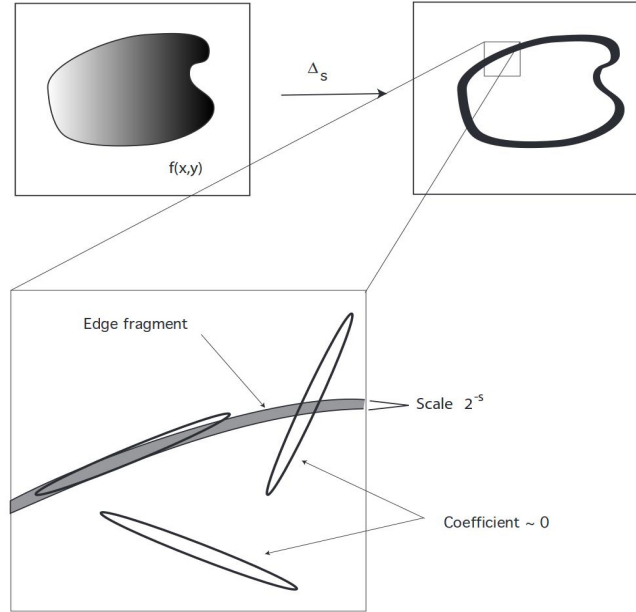


Figure 1: Edge fragment is represented by multi-scale curvelets. Unaligned coefficients are tending towards zero[10].

Most medical images generated contain curve singularities or line-like edges that often represent clinically valuable information required for diagnosis, management and to monitor progression of disease as well as efficacy of treatment. For any application that involves quantitative and qualitative assessment of imaging information beyond visual inspection, there is a need for the extraction and analysis of features such as, but not limited to, organ or tissue boundaries, vascularization, tumor margins, etc. Delineating such features of interest in ultrasound images, for the purpose of segmentation, is an especially challenging task without the expert supervision of an experienced operator. Noble et al. provide an in-depth review of the techniques used[43]. Curvelet transform was introduced by Cands et al. as a new multiresolution decomposition approach that has proved to be much more efficient at representation of edges along the curve, as compared to traditional wavelets[11]. An in-depth appreciation of the mechanics of curvelet transform is beyond the scope of this paper. For more information, refer to the detailed works of Cands, Donoho and Starck.

In the realm of medical imaging, curvelets have seen some specific uses. Applications ranging from retinal image analysis[38], MR-CT image fusion[2], mammogram classification for detection of breast cancer[20], image denoising and segmentation and classification in CT[3, 18] are some of the standout uses. Towards its use in the ultrasound segmentation problem for rotator cuff, Gupta et al., present a promising approach towards automatic segmentation of the supraspinatus[27]. But so far in our review of pertinent literature, we have not yet seen an approach similar to ours applied to this particular problem. In an attempt to address this, in the following sections we present our novel algorithmic method as well as the results on selected datasets to prove our proof-of-concept.

A.2 Methods

An algorithmic overview of the method we apply is shown in Figure 2. Although our ultimate goal is to synthesize a fully automatic segmentation and classification method, it is a two-step process. In this work, the scope of our methods is limited to the segmentation of relevant features using minimal user input. The first step involves the selection of a region of interest (ROI) which will best capture the features most relevant to our application. Apart from this, in its current implementation, the user is asked to locate two seed points. The supraspinatus is compressed between the bursae at the top and the humerus in the bottom. Both of these appear hyperechoic in the ultrasound image. The seed points are placed, one each, approximately on the left extremities of both of these components as they appear in the image. No further input is required from the user. We then utilize the curvelet transform in its discrete implementation in the form of the Fast Discrete Curvelet Transform (FDCT)[8, 9].

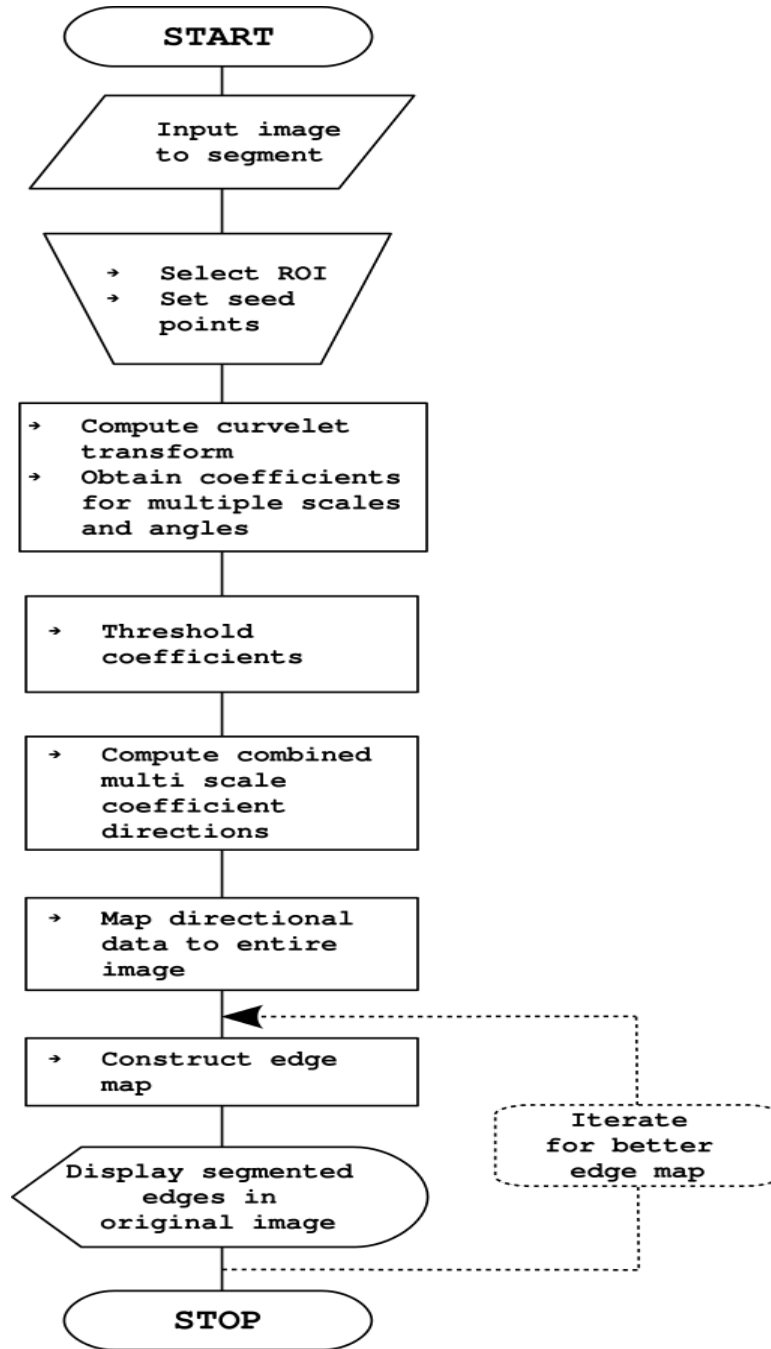


Figure 2: Algorithmic representation of ultrasound segmentation scheme.

The extracted ROI is subjected to FDCT where the image is decomposed at multiple resolutions (scales) and number of angles (orientations) at each resolution.

This generates a bank of sub bands at different scales done by spatial band pass filtering. Curvelet coefficients at scale j and angle l are represented by a matrix C_{jl} , and scale j is from finest to coarsest scale. For an image $f(x, y)$, $1 \leq t_1 \leq N_1, 1 \leq t_2 \leq N_2$, where N_1, N_2 is the size of the original image, the number of scales is calculated by

$$N_{scales} = \text{ceil}(\log_2(\min(N_1, N_2)) - 3) \quad (1)$$

The number of angles at scales $j = 2, 3, \dots, (N_{scales} - 1)$ is calculated by

$$l_j = 16 \times 2^{\text{ceil}(\frac{N_{scales}-1}{2})} \quad (2)$$

For scale $j = 2, 3, \dots, (N_{scales} - 1)$, the curvelets are divided into quadrants and are further subdivided into angular panels. For simplicity purposes, the number of angle at scale 4 is 32, at scale 3 is 32, and at scale 2 is 16. After curvelet decomposition, the low-frequency components from the image are assigned to the coarse level, the high-frequency to the fine level, and the middle frequencies contain the detail information.

The curvelet coefficients are then subjected to thresholding in order to eliminate the high frequency data which is typically associated with small scale features and noise. This is represented by smaller curvelet coefficients. We perform a hard thresholding adapting to the scale. At finer scale we eliminate more coefficients.

Once the curvelet coefficients are reduced, we then extract the directions for the highest coefficients at every scale by following the methods described by Gebck et al[23]. This describes the large scale features that are of importance and is influenced by the scale levels selected. Each curvelet C_{jl} is associated with a direction (angle) indexed by l . From (1) and (2) it is clear that the number of angles vary with the individual scale levels and hence the coefficients on the coarser level need to be mapped

to the coefficients on the finer level that they overlap. The fields are only computed for angles l up to $L/2$, where L is the total number of angles for a given scale. This is so because the other half of the angles represent the same direction. Every selected scale level has a grid of curvelet coefficients, the size of which is determined by the curvelet transform and is smaller than the size of the image. The directional fields are only computed at this grid and do not correspond to individual image pixels (Figure 3).

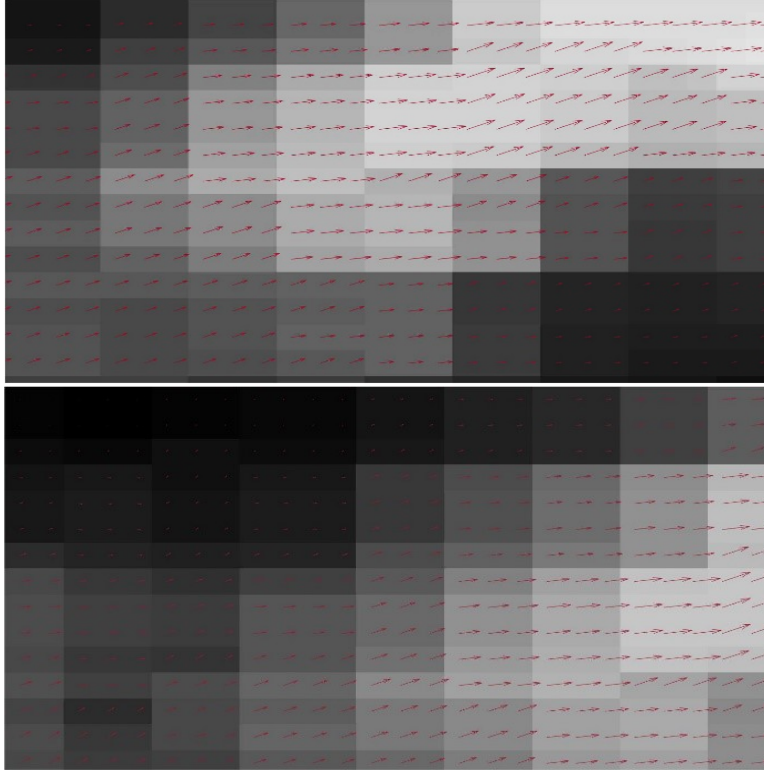


Figure 3: Directional fields along the feature. In top image the field exhibits a high degree of alignment along the edge as opposed to the curvelets away from the edge in the bottom image.

Once the directional fields are obtained, we then map them to the original

image by interpolation. This now gives us directional fields corresponding to every pixel in the image. The scale for interpolation is obtained as the ratio of the perimeters of the original image and the directional field grid. Following the interpolation step, the seed points obtained from the user during ROI selection are used as the starting point for the evolution of the curve tracing the edge. The propagation of this curve is guided by a combined intensity-direction profile based approach. The direction fields align themselves along an edge by the virtue of the mechanics of the curvelet transform. At the same time, edges are representing as an abrupt change in intensity values in the spatial domain.

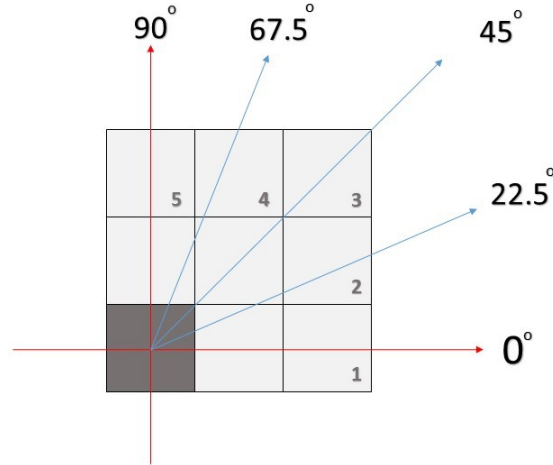


Figure 4: Illustration of combined intensity-direction profile.

The goal of the intensity-direction profile is to select the next pixel for the propagation of the curve tracing the edge. In order to do this, the average direction is first calculated over a grid of size g such that our seed pixel is at the center as

illustrated in Figure 4. Once the direction of propagation is arrived at, the next seed pixel is selected based on intensity value by comparison to its adjacent pixel. Controlling the grid size g gives finer control so as to capture smaller changes in direction of the edge. The number of iterations control the edge length traced and this can be set arbitrarily for best results.

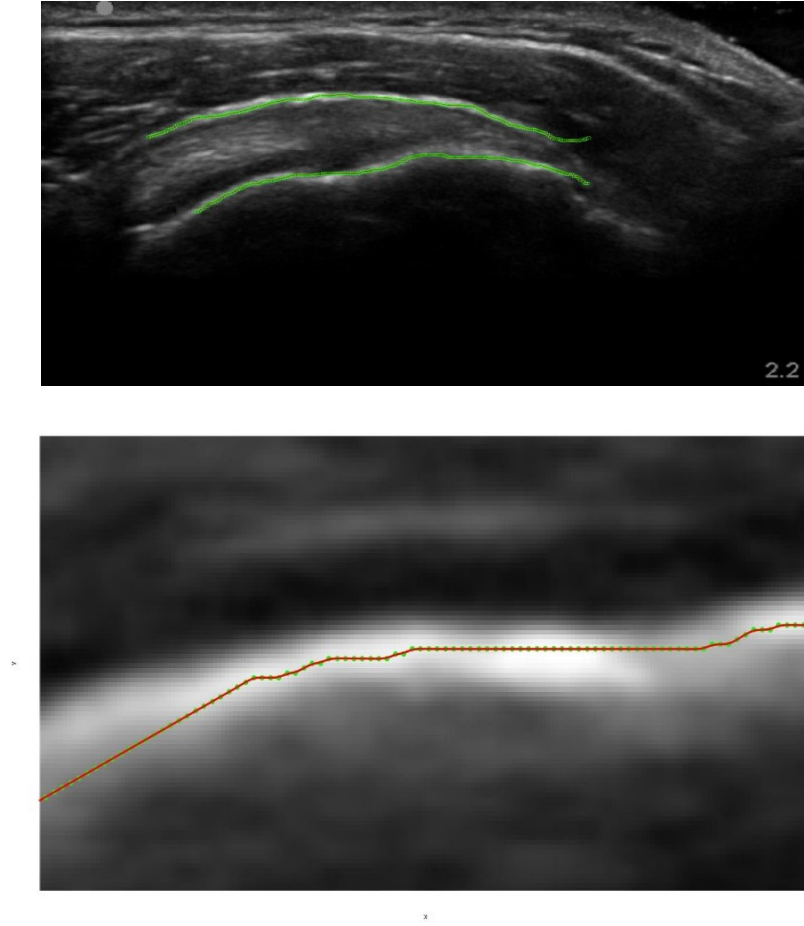


Figure 5: Segmented edge overlaid on original image (top). Magnified view of the edge showing control points that can be used for various curve fitting methods (bottom).

A.3 Results and Discussion

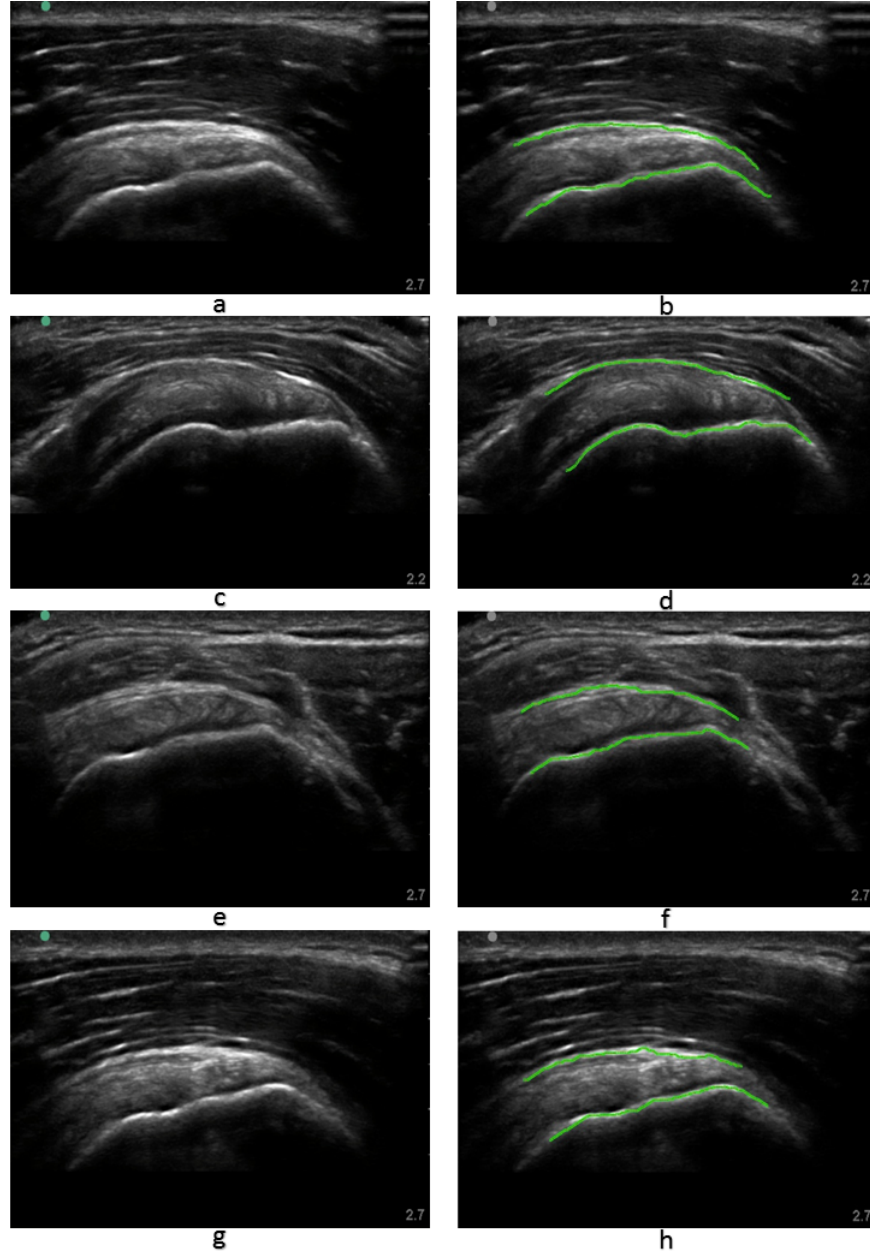


Figure 6: The left column shows the set of input images (a), (c), (e), and (g) and the right column shows the segmented edge shapes over laid on the original images (b), (d), (f), and (h).

In this paper, we have attempted to address step one of a two part problem of segmentation and classification of the supraspinatus in ultrasound imaging. This is a crucial step towards the goal of automatic classification and subsequent computation of the biomechanical properties of the supraspinatus using the ultrasound elastography techniques we have developed. The elegance of this approach lies in its simplicity when compared to the results we have demonstrated in the preceding section. Supraspinatus shows variation in terms of length, thickness and the radius of curvature among the population; however, the convex hull of the tissue remains an invariant feature. In addition to this, the tissue striations are highly directional. In our algorithm, we take advantage of these salient features and employ the curvelet transform for analysis in an area that it excels. The highly directional field we obtain from multiresolution decomposition is very sensitive to changes in the feature profile as seen in Figure 5. We supplement this information with intensity profile in the direction of the field to devise a method that is responsive to even subtle changes in the edge direction. This is demonstrated in Figure 6 (g) and (h). On close observation, one can notice the small changes in edge direction along the cortical bone of the humerus (g). These changes are captured very well in the curve, tracing the edge as detected by our algorithm (h). Figure 6 (e) and (f), demonstrates the ability of our algorithm to handle the smoother changes in curvature.

It is important to note that prior to running the algorithm on the images, they were not subject to any preprocessing. And although the ROI selection can be viewed as a preprocessing step, it is worthy to observe that our method is quite immune to noise in the image. This is another inherent key feature of the curvelet transform. The process of thresholding the coefficients is the crux of image denoising algorithms that are implemented using curvelets. In the current implementation, we use hard thresholding approach and believe we could only improve this step by

employing more advanced techniques; one such technique used in wavelet denoising is the Total Variation (TV) thresholding.

In the introduction section, we underlined that our final goal is to develop a fully automatic segmentation technique. But having developed the ability to reliably extract edge information, we can now perform comparative studies to quantitatively measure the efficacy of segmentation as compared to an experienced clinical operator. This will allow us to build confidence in acquiring data to establish ground truth which is required to implement probabilistic and heuristic techniques for automatic segmentation. One such example is the possible use of Statistical Shape Modeling (SSM) to predict the shape of the tissue in an ultrasound image. It is also noteworthy that although in this current implementation we require user input, in the framework of a clinical workflow for the current application, the time taken to perform this task is insignificant.

The current implementation in Matlab, although quick, may not be suitable for a real time application. However with the C++ implementation of the curvelet transform made available[9], it would be beneficial to implement a computationally optimized form of this algorithm so that it can be utilized for real time applications.

Bibliography

- [1] Consortium for Radiologic Imaging Studies of Polycystic Kidney Disease (CRISP).
- [2] F E Ali, I M El-Dokany, A A Saad, and Fathi El-Sayed Abd El-Samie. Curvelet fusion of MR and CT images. *Progress In Electromagnetics Research C*, 3:215–224, 2008.
- [3] Shadi AlZubi, Naveed Islam, and Maysam Abbod. Multiresolution analysis using wavelet, ridgelet, and curvelet transforms for medical image segmentation. *Journal of Biomedical Imaging*, 2011:4, 2011.
- [4] Kyongtae T Bae, Cheng Tao, Fang Zhu, James E Bost, Arlene B Chapman, Jared J Grantham, Vicente E Torres, Lisa M Guay-Woodford, Catherine M Meyers, William M Bennett, and Others. MRI-based kidney volume measurements in ADPKD: reliability and effect of gadolinium enhancement. *Clinical Journal of the American Society of Nephrology*, 4(4):719–725, 2009.
- [5] Jeannette Bakker, Marco Olree, Robert Kaatee, Eduard E de Lange, Karel G M Moons, Jaap J Beutler, and Frederik J A Beek. Renal volume measurements: accuracy and repeatability of US compared with that of MR Imaging 1. *Radiology*, 211(3):623–628, 1999.
- [6] Kline Bolton, Bruce Culleton, K Harvey, and Others. K/DOQI clinical practice guidelines for chronic kidney disease: evaluation, classification, and stratification. Kidney Disease Outcome Quality Initiative. *Am J Kidney Dis*, 39(2 Suppl 1):S1–246, 2002.
- [7] Peter Boor, Tammo Ostendorf, and Jürgen Floege. Renal fibrosis: novel insights into mechanisms and therapeutic targets. *Nature Reviews Nephrology*, 6(11):643–656, 2010.
- [8] Emmanuel Candes, Laurent Demanet, David Donoho, and Lexing Ying. Fast discrete curvelet transforms. *Multiscale Modeling & Simulation*, 5(3):861–899, 2006.

- [9] Emmanuel J Candès, Laurent Demanet, David L Donoho, and Lexing Ying. Implementation of Fast Discrete Curvelet Transform.
- [10] Emmanuel J Candès and David L Donoho. New tight frames of curvelets and optimal representations of objects with piecewise C2 singularities. *Communications on pure and applied mathematics*, 57(2):219–266, 2004.
- [11] Emmanuel J Candes and David L Donoho. Continuous curvelet transform: II. Discretization and frames. *Applied and Computational Harmonic Analysis*, 19(2):198–222, 2005.
- [12] Guillermo Carbajal, Andras Lasso, Álvaro Gómez, and Gabor Fichtinger. Improving N-wire phantom-based freehand ultrasound calibration. *International journal of computer assisted radiology and surgery*, 8(6):1063–1072, 2013.
- [13] David M Cash, Michael I Miga, Sean C Glasgow, Benoit M Dawant, Logan W Clements, Zhujiang Cao, Robert L Galloway, and William C Chapman. Concepts and preliminary data toward the realization of image-guided liver surgery. *Journal of Gastrointestinal Surgery*, 11(7):844–859, 2007.
- [14] Arlene B Chapman, James E Bost, Vicente E Torres, Lisa Guay-Woodford, Kyongtae Ty Bae, Douglas Landsittel, Jie Li, Bernard F King, Diego Martin, Louis H Wetzel, and Others. Kidney volume and functional outcomes in autosomal dominant polycystic kidney disease. *Clinical Journal of the American Society of Nephrology*, 7(3):479–486, 2012.
- [15] Arlene B Chapman, Lisa M Guay-Woodford, Jared J Grantham, Vicente E Torres, Kyongtae T Bae, Deborah A Baumgarten, Philip J Kenney, Bernard F King Jr, James F Glockner, Louis H Wetzel, Marijn E Brummer, W Charles O’Neill, Michelle L Robbin, William M Bennett, Saulo Klahr, Gladys H Hirschman, Paul L Kimmel, Paul A Thompson, and J Philip Miller. Renal structure in early autosomal-dominant polycystic kidney disease (ADPKD): The Consortium for Radiologic Imaging Studies of Polycystic Kidney Disease (CRISP) cohort1. *Kidney International*, 64(3):1035–1045, 2003.
- [16] Benjamin Cheong, Raja Muthupillai, Mario F Rubin, and Scott D Flamm. Normal values for renal length and volume as measured by magnetic resonance imaging. *Clinical Journal of the American Society of Nephrology*, 2(1):38–45, 2007.
- [17] Kevin Cleary and Terry M Peters. Image-guided interventions: technology review and clinical applications. *Annual review of biomedical engineering*, 12:119–42, aug 2010.
- [18] Lucia Dettori and Lindsay Semler. A comparison of wavelet, ridgelet, and curvelet-based texture classification algorithms in computed tomography. *Computers in Biology and Medicine*, 37(4):486–498, 2007.

- [19] Robert Elfring, Mat\`ias de la Fuente, and Klaus Radermacher. Assessment of optical localizer accuracy for computer aided surgery systems. *Computer Aided Surgery*, 15(1-3):1–12, 2010.
- [20] Mohamed Meselhy Eltoukhy, Ibrahima Faye, and Brahim Belhaouari Samir. Breast cancer diagnosis in digital mammogram using multiscale curvelet transform. *Computerized medical imaging and graphics*, 34(4):269–276, 2010.
- [21] Andriy Fedorov, Reinhard Beichel, Jayashree Kalpathy-Cramer, Julien Finet, Jean-Christophe Fillion-Robin, Sonia Pujol, Christian Bauer, Dominique Jennings, Fiona Fennessy, Milan Sonka, and Others. 3D Slicer as an image computing platform for the Quantitative Imaging Network. *Magnetic resonance imaging*, 30(9):1323–1341, 2012.
- [22] Alfred M Franz, Tamas Haidegger, Wolfgang Birkfellner, Kevin Cleary, Terry M Peters, and Lena Maier-Hein. Electromagnetic tracking in medicine a review of technology, validation, and applications. *IEEE transactions on medical imaging*, 33(8):1702–1725, 2014.
- [23] Tobias Gebäck and Petros Koumoutsakos. Edge detection in microscopy images using curvelets. *BMC bioinformatics*, 10(1):75, 2009.
- [24] Jared J Grantham. Autosomal dominant polycystic kidney disease. *New England Journal of Medicine*, 359(14):1477–1485, 2008.
- [25] Jared J Grantham, Sumanth Mulamalla, and Katherine I Swenson-Fields. Why kidneys fail in autosomal dominant polycystic kidney disease. *Nature Reviews Nephrology*, 7(10):556–566, 2011.
- [26] Jared J Grantham, Vicente E Torres, Arlene B Chapman, Lisa M Guay-Woodford, Kyongtae T Bae, Bernard F King Jr, Louis H Wetzel, Deborah A Baumgarten, Phillip J Kenney, Peter C Harris, and Others. Volume progression in polycystic kidney disease. *New England Journal of Medicine*, 354(20):2122–2130, 2006.
- [27] Rishu Gupta, Irraivan Elamvazuthi, Sarat C Dass, Ibrahima Faye, Pandian Vasant, John George, and Faizatul Izza. Curvelet based automatic segmentation of supraspinatus tendon from ultrasound image: a focused assistive diagnostic method. *Biomedical engineering online*, 13(1):157, 2014.
- [28] TC Hart, MC Gorry, PS Hart, AS Woodard, Z Shihabi, J Sandhu, B Shirts, L Xu, H Zhu, MM Barmada, et al. Mutations of the umod gene are responsible for medullary cystic kidney disease 2 and familial juvenile hyperuricaemic nephropathy. *Journal of medical genetics*, 39(12):882–892, 2002.

- [29] Inge A Hoevenaren, Ruth Wester, Robert W Schrier, Kim McFann, R Brian Doctor, Joost PH Drenth, and Gregory T Everson. Polycystic liver: clinical characteristics of patients with isolated polycystic liver disease compared with patients with polycystic liver and autosomal dominant polycystic kidney disease. *Liver International*, 28(2):264–270, 2008.
- [30] Po-Wei Hsu, Richard W Prager, Andrew H Gee, and Graham M Treece. Free-hand 3d ultrasound calibration: a review. In *Advanced imaging in biology and medicine*, pages 47–84. Springer, 2009.
- [31] Johann B Hummel, Michael R Bax, Michael L Figl, Yan Kang, Calvin Maurer, Wolfgang W Birkfellner, Helmar Bergmann, and Ramin Shahidi. Design and application of an assessment protocol for electromagnetic tracking systems. *Medical physics*, 32(7):2371–2379, 2005.
- [32] David Kwartowitz, Erika Trent, Fuad Meffeh, Vipul Pai Raikar, and Delphine Dean. Devices that cooperate with ultrasound probes for musculoskeletal evaluations and related systems and methods, 2013.
- [33] Andras Lasso, Tamas Heffter, Adam Rankin, Csaba Pinter, Tamas Ungi, and Gabor Fichtinger. PLUS: Open-source toolkit for ultrasound-guided intervention systems. *IEEE Transactions on Biomedical Engineering*, (10):2527–2537, oct 2014.
- [34] E D Light, R E Davidsen, J O Fiering, T A Hruschka, and S W Smith. Progress in two-dimensional arrays for real-time volumetric imaging. *Ultrasonic imaging*, 20(1):1–15, 1998.
- [35] Marcel Lüthi, Remi Blanc, Thomas Albrecht, Tobias Gass, Orcun Goksel, Philippe Büchler, Michael Kistler, Habib Bousleiman, Mauricio Reyes, Philippe Cattin, and Others. Statismo-A framework for PCA based statistical models. *The Insight Journal*, 1:1–18, 2012.
- [36] Marcel Lüthi, Christoph Jud, Thomas Gerig, and Thomas Vetter. Gaussian Process Morphable Models. *arXiv preprint arXiv:1603.07254*, 2016.
- [37] Marcel Lüthi, Christoph Jud, and Thomas Vetter. A unified approach to shape model fitting and non-rigid registration. In *Machine learning in medical imaging*, pages 66–73. Springer, 2013.
- [38] Mohammad Saleh Miri and Ali Mahloojifar. Retinal image analysis using curvelet transform and multistructure elements morphology by reconstruction. *Biomedical Engineering, IEEE Transactions on*, 58(5):1183–1192, 2011.

- [39] Thida M Myint, Gopi K Rangan, and Angela C Webster. Treatments to slow progression of autosomal dominant polycystic kidney disease: systematic review and meta-analysis of randomized trials. *Nephrology*, 19(4):217–226, 2014.
- [40] Andriy Myronenko and Xubo Song. Point set registration: Coherent point drift. *Pattern Analysis and Machine Intelligence, IEEE Transactions on*, 32(12):2262–2275, 2010.
- [41] Andriy Myronenko, Xubo Song, Miguel A Carreira-Perpinán, et al. Non-rigid point set registration: Coherent point drift. *Advances in Neural Information Processing Systems*, 19:1009, 2007.
- [42] Surya M Nauli, Francis J Alenghat, Ying Luo, Eric Williams, Peter Vassilev, Xiaogang Li, Andrew E H Elia, Weining Lu, Edward M Brown, Stephen J Quinn, and Others. Polycystins 1 and 2 mediate mechanosensation in the primary cilium of kidney cells. *Nature genetics*, 33(2):129–137, 2003.
- [43] J Alison Noble and Djamal Boukerroui. Ultrasound image segmentation: a survey. *Medical Imaging, IEEE Transactions on*, 25(8):987–1010, 2006.
- [44] W Charles O’Neill, Michelle L Robbin, Kyongtae T Bae, Jared J Grantham, Arlene B Chapman, Lisa M Guay-Woodford, Vicente E Torres, Bernard F King, Louis H Wetzel, Paul A Thompson, and Others. Sonographic assessment of the severity and progression of autosomal dominant polycystic kidney disease: the Consortium of Renal Imaging Studies in Polycystic Kidney Disease (CRISP). *American journal of kidney diseases*, 46(6):1058–1064, 2005.
- [45] R D Perrone, J F Marier, M S Mouksassi, F Czerwiec, K Romero, E Dennis, D Miskulin, A Chapman, B Gitomer, and V Torres. Qualification of total kidney volume as a prognostic biomarker for use in clinical trials evaluating patients with autosomal dominant polycystic kidney disease. In *AMERICAN JOURNAL OF KIDNEY DISEASES*, volume 63, pages A119—A119. WB SAUNDERS CO-ELSEVIER INC 1600 JOHN F KENNEDY BOULEVARD, STE 1800, PHILADELPHIA, PA 19103-2899 USA, 2014.
- [46] Anup Pillai, Brittany N Hall, Charles A Thigpen, and David M Kwartowitz. Improved apparatus for predictive diagnosis of rotator cuff disease. In *SPIE Medical Imaging*, page 904005. International Society for Optics and Photonics, 2014.
- [47] Richard W Prager, Andrew H Gee, Graham M Treece, Charlotte JC Cash, and Laurence H Berman. Sensorless freehand 3-d ultrasound using regression of the echo intensity. *Ultrasound in medicine & biology*, 29(3):437–446, 2003.

- [48] Qi Qian, Airong Li, Bernard F King, Patrick S Kamath, Donna J Lager, John Huston, Clarence Shub, Sonia Davila, Stefan Somlo, and Vicente E Torres. Clinical profile of autosomal dominant polycystic liver disease. *Hepatology*, 37(1):164–171, 2003.
- [49] Berenice Reed, Kim McFann, William J Kimberling, York Pei, Patricia A Gabow, Karen Christopher, Eric Petersen, Catherine Kelleher, Pamela R Fain, Ann Johnson, et al. Presence of de novo mutations in autosomal dominant polycystic kidney disease patients without family history. *American Journal of Kidney Diseases*, 52(6):1042–1050, 2008.
- [50] Scott Reule, Donal J Sexton, Craig A Solid, Shu-Cheng Chen, Allan J Collins, and Robert N Foley. ESRD from autosomal dominant polycystic kidney disease in the United States, 2001-2010. *American Journal of Kidney Diseases*, 64(4):592–599, 2014.
- [51] Robert Rohling, Wilson Fung, and Pedram Lajevardi. PUPIL: Programmable ultrasound platform and interface library. In *International Conference on Medical Image Computing and Computer-Assisted Intervention*, pages 424–431. Springer, 2003.
- [52] Matthew Tan, Hiromi I Wettersten, Kristy Chu, David L Huso, Terry Watnick, Sharon Friedlander, Yosef Landesman, and Robert H Weiss. Novel inhibitors of nuclear transport cause cell cycle arrest and decrease cyst growth in ADPKD associated with decreased CDK4 levels. *American Journal of Physiology-Renal Physiology*, 307(11):F1179—F1186, 2014.
- [53] Vicente E Torres, Arlene B Chapman, Olivier Devuyst, Ron T Gansevoort, Jared J Grantham, Eiji Higashihara, Ronald D Perrone, Holly B Krasa, John Ouyang, and Frank S Czerwiec. Tolvaptan in patients with autosomal dominant polycystic kidney disease. *New England Journal of Medicine*, 367(25):2407–2418, 2012.
- [54] Vicente E Torres, Peter C Harris, and Yves Pirson. Autosomal dominant polycystic kidney disease. *The Lancet*, 369(9569):1287–1301, 2007.
- [55] Vicente E Torres, Bernard F King, Arlene B Chapman, Marijn E Brummer, Kyongtae T Bae, James F Glockner, Kraisthith Arya, Dana Risk, Joel P Felmlee, Jared J Grantham, and Others. Magnetic resonance measurements of renal blood flow and disease progression in autosomal dominant polycystic kidney disease. *Clinical Journal of the American Society of Nephrology*, 2(1):112–120, 2007.
- [56] VICENTE E TORRES, DAVID M WILSON, JOHN C BURNETT, CHRISTOPHER M JOHNSON, and KENNETH P OFFORD. Effect of inhibition of converting enzyme on renal hemodynamics and sodium management in polycystic

- kidney disease. In *Mayo Clinic Proceedings*, volume 66, pages 1010–1017. Elsevier, 1991.
- [57] VICENTE E TORRES, DAVID M WILSON, KENNETH P OFFORD, JOHN C BURNETT, and JUAN C ROMERO. Natriuretic response to volume expansion in polycystic kidney disease. In *Mayo Clinic Proceedings*, volume 64, pages 509–515. Elsevier, 1989.
 - [58] Erika A Trent, Lane Bailey, Fuad N Mefleh, Vipul P Raikar, Ellen Shanley, Charles A Thigpen, Delphine Dean, and David M Kwartowitz. Assessment and characterization of in situ rotator cuff biomechanics. In *Proc. SPIE*, volume 8672, pages 86721M—86721M. International Society for Optics and Photonics, 2013.
 - [59] Theresa A Tuthill, JF Krücker, J Brian Fowlkes, and Paul L Carson. Automated three-dimensional us frame positioning computed from elevational speckle decorrelation. *Radiology*, 209(2):575–582, 1998.
 - [60] Andrew D Wiles, David G Thompson, and Donald D Frantz. Accuracy assessment and interpretation for optical tracking systems. In *Medical Imaging 2004*, pages 421–432. International Society for Optics and Photonics, 2004.
 - [61] Hubert Wong, Laura Vivian, Gabrielle Weiler, and Guido Filler. Patients with autosomal dominant polycystic kidney disease hyperfiltrate early in their disease. *American journal of kidney diseases*, 43(4):624–628, 2004.
 - [62] Claire Woon, Ashleigh Bielinski-Bradbury, Karl O’Reilly, and Paul Robinson. A systematic review of the predictors of disease progression in patients with autosomal dominant polycystic kidney disease. *BMC nephrology*, 16(1):1, 2015.
 - [63] W Wynn, C Frahm, P Carroll, R Clark, J Wellhoner, and M Wynn. Advanced superconducting gradiometer/magnetometer arrays and a novel signal processing technique. *IEEE Transactions on Magnetism*, 11(2):701–707, 1975.
 - [64] Ziv Yaniv, Emmanuel Wilson, David Lindisch, and Kevin Cleary. Electromagnetic tracking in the clinical environment. *Medical Physics*, 36(3):876, 2009.
 - [65] Cha Zhang and Tsuhan Chen. Efficient feature extraction for 2D/3D objects in mesh representation. In *Image Processing, 2001. Proceedings. 2001 International Conference on*, volume 3, pages 935–938. IEEE, 2001.